Cell Reports
Physical Science

CellPress
OPEN ACCESS

Article

Ultrasensitive and Selective Detection of SARS-CoV-2 Using Thermotropic Liquid Crystals and Image-Based Machine Learning

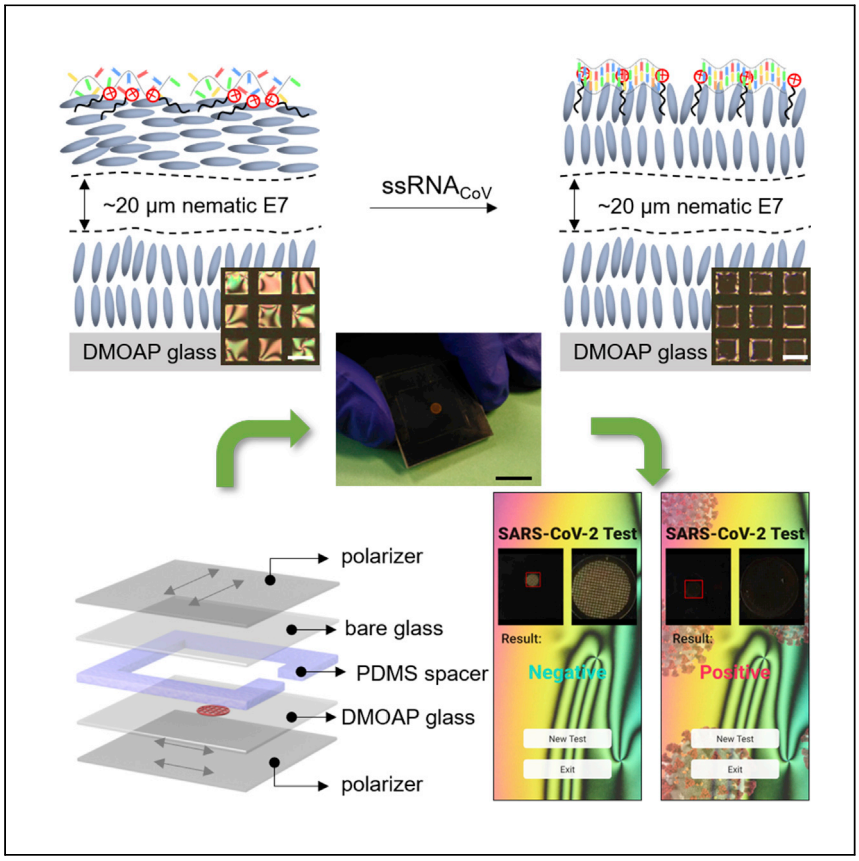

Xu et al. report that surfactant-laden liquid crystal (LC) films can detect ssRNA of SARS-CoV-2 with high selectivity and sensitivity. Combing polarized light microscopy work principle and machine learning technology, a LC-based diagnostic kit and a smartphone-based application (app) are developed to enable automatic detection of SARS-CoV-2 ssRNA.

Yang Xu, Adil M. Rather, Shuang Song, ..., Rongjun Qin, Xiaoping Bao, Xiaoguang Wang

qin.324@osu.edu (R.Q.)
bao61@purdue.edu (X.B.)
wang.12206@osu.edu (X.W.)

HIGHLIGHTS

Detection of ssRNA of SARS-CoV-2 using surfactant-laden liquid crystal (LC) films

Precise detection of nucleotide sequence with high selectivity and sensitivity

Develop LC-based diagnostic kit for naked-eye detection of SARS-CoV-2 ssRNA

Develop a smartphone application (app) to enable automatic detection of SARS-CoV-2 ssRNA

Xu et al., Cell Reports Physical Science 1, 100276
December 23, 2020
https://doi.org/10.1016/j.xcrp.2020.100276

Cell Reports
Physical Science

CellPress
OPEN ACCESS

Article

Ultrasensitive and Selective Detection of SARS-CoV-2 Using Thermotropic Liquid Crystals and Image-Based Machine Learning

Yang Xu,[1,7] Adil M. Rather,[1,7] Shuang Song,[2,7] Jen-Chun Fang,[1] Robert L. Dupont,[1] Ufuoma I. Kara,[1] Yun Chang,[3] Joel A. Paulson,[1,4] Rongjun Qin,[2,5,6,*] Xiaoping Bao,[3,*] and Xiaoguang Wang[1,4,8,*]

SUMMARY

Rapid, robust virus-detection techniques with ultrahigh sensitivity and selectivity are required for the outbreak of the pandemic coronavirus disease 2019 (COVID-19) caused by the severe acute respiratory syndrome-coronavirus-2 (SARS-CoV-2). Here, we report that the femtomolar concentrations of single-stranded ribonucleic acid (ssRNA) of SARS-CoV-2 trigger ordering transitions in liquid crystal (LC) films decorated with cationic surfactant and complementary 15-mer single-stranded deoxyribonucleic acid (ssDNA) probe. More importantly, the sensitivity of the LC to the SARS ssRNA, with a 3-bp mismatch compared to the SARS-CoV-2 ssRNA, is measured to decrease by seven orders of magnitude, suggesting that the LC ordering transitions depend strongly on the targeted oligonucleotide sequence. Finally, we design a LC-based diagnostic kit and a smartphone-based application (app) to enable automatic detection of SARS-CoV-2 ssRNA, which could be used for reliable self-test of SARS-CoV-2 at home without the need for complex equipment or procedures.

INTRODUCTION

The outbreak of the coronavirus disease 2019 (COVID-19), caused by the novel severe acute respiratory syndrome-coronavirus-2 (SARS-CoV-2) virus, has spread rapidly and evolved into a global pandemic.[1–3] SARS-CoV-2 has an incubation period of 2–7 days, during which infected individuals present no obvious symptoms,[4,5] and the transmission of the SARS-CoV-2 virus has been shown to peak on or before symptom onset.[6,7] To efficiently control such pre-symptomatic transmission, rapid, robust, and inexpensive tests should be performed on a large fraction of the population.[3,8] Nucleic acid tests on the viral RNAs swabbed from a patient's throat or nasal passage, typically in the form of a reverse-transcription polymerase chain reaction (RT-PCR) test, are effective for the detection of the SARS-CoV-2 virus. This RT-PCR test is considered to be the "gold standard" for clinical diagnosis.[8–10] A promising alternative approach to RT-PCR is the isothermal amplification method, which mainly contains two techniques: loop-mediated isothermal amplification (LAMP)[11] and recombinase polymerase amplification (RPA).[12] However, these methods require both long characterization time and specialized equipment.

Very recently, Cas12 and Cas13,[13] gold nanoparticles,[14] field-effect transistors (FETs),[15] the plasmonic photothermal (PPT) effect,[16] and column agglutination test (CAT) technologies[17] have emerged as diagnostic tools for the detection of SARS-CoV-2. Although these diagnostic techniques are promising, each has its

[1]William G. Lowrie Department of Chemical and Biomolecular Engineering, The Ohio State University, Columbus, OH 43210, USA

[2]Department of Civil, Environmental and Geodetic Engineering, The Ohio State University, Columbus, OH 43210, USA

[3]Davidson School of Chemical Engineering, Purdue University, West Lafayette, IN 47907, USA

[4]Sustainability Institute, The Ohio State University, Columbus, OH 43210, USA

[5]Department of Electrical and Computer Engineering, The Ohio State University, Columbus, OH 43210, USA

[6]Translational Data Analytics Institute, The Ohio State University, Columbus, OH 43210, USA

[7]These authors contributed equally

[8]Lead Contact

*Correspondence: qin.324@osu.edu (R.Q.), bao61@purdue.edu (X.B.), wang.12206@osu.edu (X.W.)

https://doi.org/10.1016/j.xcrp.2020.100276

own limitations. For example, the gold-nanoparticle-based technique is cost prohibitive for large-scale testing and requires improvements in its detection limit in order to reduce the required input amount of virus samples. Moreover, the FETs and PPT-effect-based diagnostic approaches require specialized analytical equipment for virus detection, and the CAT approach requires blood sample collection and centrifugation that depends on an established testing laboratory. Thus, the development of a low-cost, rapid, reliable, and simple diagnostic method for the self-detection of the SARS-CoV-2 virus remains elusive.

Thermotropic liquid crystals (LCs) exhibit unifying characteristics and behaviors that emerge from the long-range orientational order and mobility of their mesogenic constituents[18,19] and have been broadly utilized in fast-switching electro-optical devices, such as liquid crystal displays (LCDs).[20] Over the past decade, a series of work has revealed the design of LC films and droplets that undergo orientational ordering transitions in response to a wide range of molecules adsorbed at an interface, including synthetic surfactants[21–23] and polymers,[24,25] phospholipids,[26–29] peptides,[30] proteins,[31–34] streptavidin,[35] bacterial toxins,[36] and deoxyribonucleic acid (DNA).[37–41] For instance, single-stranded DNA (ssDNA) and double-stranded DNA (dsDNA) produce different orientations of LCs at cationic surfactant-laden aqueous-LC interfaces, which leads to a change in the effect on visible light caused by the optical birefringence of the LC film and thus enables the detection of DNA hybridization under polarized light microscopy.[40,41] Despite the great potential of LC biosensor applications, their rational study and use in the detection of ribonucleic acid (RNA), which is the core genetic material of most pathogenic viruses, have not yet been explored.

In this study, we report the design of LC-based sensors for the reliable detection of SARS-CoV-2 RNA. Specifically, a partially self-assembled monolayer of cationic surfactants is formed at an aqueous-LC interface, followed by the adsorption of a 15-mer ssDNA probe with a complementary sequence to the SARS-CoV-2 virus at the cationic surfactant-laden aqueous-LC interface. We demonstrate that the ordering transition in the formed LC surface strongly depends on the targeted nucleotide sequence. The minimum concentration of SARS-CoV-2 RNA that can drive an ordering transition in the LC film is seven orders of magnitude lower than that of the base-pair-mismatched SARS RNA. Furthermore, we design and fabricate a LC-based SARS-CoV-2 RNA point-of-care detection kit, with an obtained response that is visible to the naked eye without any additional equipment, and a smartphone-based application (app) to enhance the overall accuracy of the test result readout and to avoid user error. Overall, these results unmask principles by which LCs and RNA can be coupled at cationic surfactant-decorated aqueous interfaces and hint at new routes by which the RNA of a pathogenic virus can be rapidly and easily sensed using LCs with both high sensitivity and selectivity.

RESULTS AND DISCUSSION

Preparation of the Cationic Surfactant-Decorated LC Films

The initial experiments reported below employed a cationic surfactant dodecyltrimethylammonium bromide (DTAB)-decorated interface on micrometer-thick films of nematic E7. The thermotropic LC E7 was chosen because of the relatively broad temperature range of its nematic mesophase (−62°C–58°C). In this phase, the rod-shaped E7 molecules have no positional order but self-align to possess a long-range orientational order. As described in the Experimental Procedures and in Figure 1, films of nematic E7, with an approximately flat interface, were prepared by filling

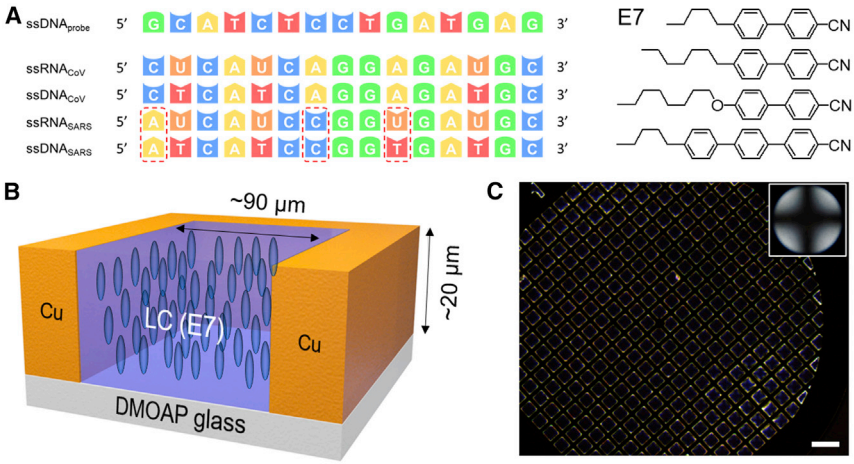

Figure 1. ssDNA/ssRNA Sequences and Grid-Infused LC Films

(A) Oligonucleotide sequence of ssDNA and ssRNA and the molecular structure of thermotropic LC E7.

(B) Schematic illustration of the E7-filled specimen grid on a DMOAP-functionalized glass slide.

(C) Representative optical micrograph (crossed polarizers) of the E7-filled specimen grid on a DMOAP-functionalized glass slide in air. Inset in (C) is a conoscopic image confirming homeotropic alignment of E7 in the film. Scale bar, 200 μm.

the pores of a 20-μm-thick copper specimen grid supported on a dimethyloctadecyl [3-(trimethoxysilyl) propyl]ammonium chloride (DMOAP)-functionalized glass slide, which induced a perpendicular ordering of the E7. Next, the E7 films were submerged into an aqueous solution of 5 mM sodium chloride (NaCl) (pH ~5.5–6.0), which was chosen to minimize the repulsive interaction of the base pairs of the ssDNA.[40]

A monolayer of DTAB was subsequently deposited at the aqueous-E7 interface by adding an aqueous solution of DTAB to the aqueous phase above the E7 film. The DTAB was then allowed to adsorb onto the surface for 10 min. The optical images of DTAB-decorated E7 films were obtained by using an Olympus BX53 polarized light microscope equipped with crossed polarizers and set to the transmission mode. After adsorption of DTAB at the aqueous-E7 interface, we observed the optical appearance of the E7 films to be uniformly dark, which is consistent with the homeotropic anchoring of the nematic E7 at the DTAB-decorated aqueous interface of the E7 films (Figure 2A). Previous studies have established that steric interactions between the acyl tails of synthetic surfactants and mesogens cause LCs to adopt a homeotropic orientation.[37,40] We comment here that, under the experimental condition of a 0.5 mM solution of DTAB, where the surface coverage of DTAB was near the minimum required for homeotropic orientation, we calculated only ~36% of the aqueous interface to be covered by DTAB (see Notes S1 and S2). These results suggest that a substantial open LC surface area exists at the interface and thus a LC reorientation is allowed upon the adsorption of ssRNA and/or ssDNA at the interface. We also comment here that such low surface coverage of DTAB plays a critical role in the ultrasensitive detection of SARS-CoV-2, which will be discussed later.

Adsorption of the Probe ssDNA

Next, we deposited a 15-mer probe ssDNA (ssDNA$_{probe}$) (5′-GCATCTCCTGATGAG-3′), which can hybridize with our target 15-mer SARS-CoV-2 ssRNA (ssRNA$_{CoV}$) (5′-CUCAUCAGGAGAUGC-3′), at the DTAB-decorated aqueous-E7 interface. The negatively charged ssDNA is attracted to the cationic DTAB at the aqueous-E7

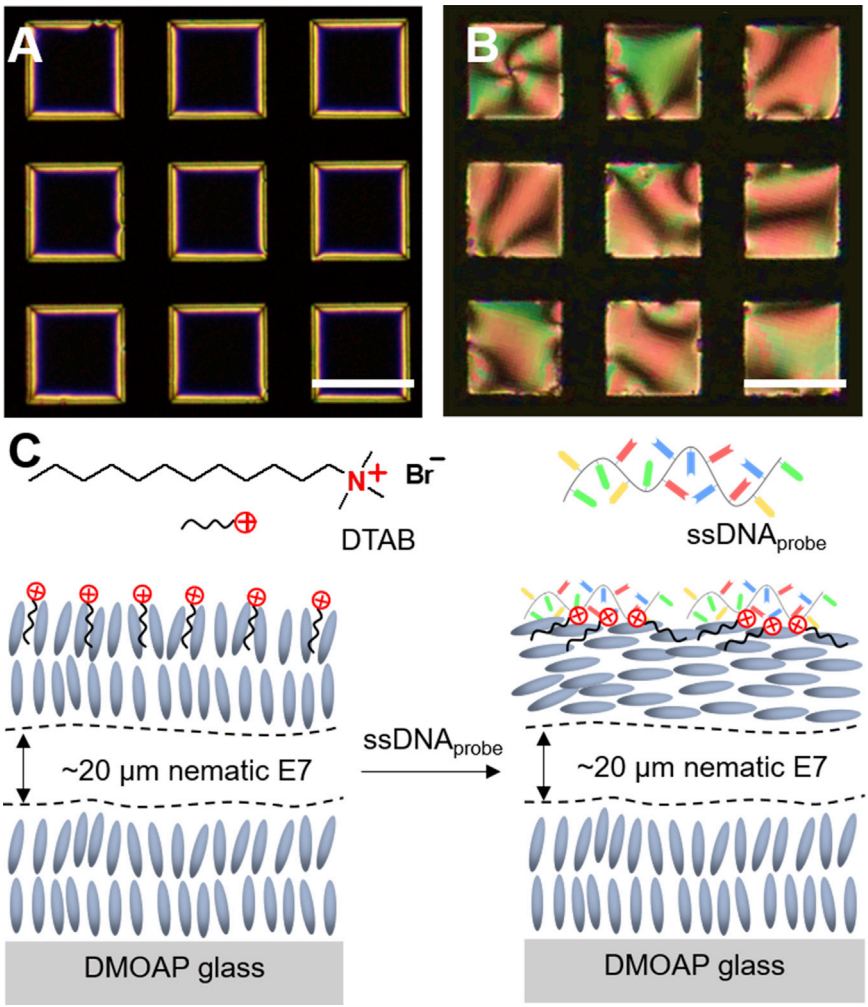

Figure 2. Adsorption of the Probe DNA at the Cationic Surfactant-Decorated Aqueous-LC Interface

(A and B) Optical micrographs (crossed polarizers) of the E7 film after the adsorption of (A) DTAB and the subsequent adsorption of (B) the $ssDNA_{probe}$. Scale bars, 100 μm.

(C) Schematic illustration of the optical response of the DTAB-decorated LC film to the adsorption of the $ssDNA_{probe}$.

interface via electrostatic interactions. The temperature of the system was kept at the melting temperature (T_m) of the $ssDNA_{probe}$, at which 50% of the nucleotide was annealed. Figure 2B shows the dynamic optical response of the DTAB-decorated nematic E7 film to the adsorption of $ssDNA_{probe}$. After addition of 100 nM $ssDNA_{probe}$, micrometer-sized domains with a bright optical appearance (corresponding to the regions of E7 with a tilted or planar alignment) nucleated at the interface. Subsequently, these domains grew over a period of 10 min, resulting in a bright optical appearance across the entire aqueous-E7 interface. These results indicate that, as the $ssDNA_{probe}$ adsorbs to the interface, the flexible $ssDNA_{probe}$ chains (with typical persistence length of ~6 Å)[42] tend to spread at the surface and the hydrophobic bases of the $ssDNA_{probe}$ interact with the DTAB to decrease the effective surface coverage of DTAB below what is required for a homeotropic orientation, resulting in a reorientation of the LC from homeotropic to either tilted or planar, as illustrated in Figure 2C. This phenomenon is consistent with previous

studies.[37,41] The concentration of the $ssDNA_{probe}$ was fixed at 100 nM for the rest of the experiments performed in this work. We emphasize here that the addition of 100 nM $ssDNA_{probe}$ to E7 films incubated in a 6 mM DTAB solution (>90% of the aqueous-E7 interface is covered by DTAB; Figure S1) triggers no measurable change in the optical appearance of the E7 films, revealing that the surface coverage of DTAB plays a key role in driving the reorientation of the LC surface anchoring upon adsorption of the $ssDNA_{probe}$.

Detection of the SARS-CoV-2 ssRNA

In this set of experiments, we investigated the effect of the adsorption of $ssRNA_{CoV}$ on the optical response of the $ssDNA_{probe}$/DTAB-decorated aqueous-E7 interfaces (Video S1). As shown in Figure 3A, after addition of the $ssRNA_{CoV}$ to the aqueous phase, black domains were observed to nucleate and grow on the E7 surface over a period of 20 min, resulting in a uniformly dark optical appearance that corresponds to the homeotropic anchoring of the nematic E7 across the entire aqueous-E7 interface. Furthermore, quantification of the optical appearance of the E7 films revealed a clear threshold concentration in a plot of normalized grayscale of E7 films versus $ssRNA_{CoV}$ concentration (Figures 3B and S2). Inspection of Figure 3D shows that remarkably low concentrations of $ssRNA_{CoV}$ (~30 fM of target ssRNA) are able to trigger the ordering transition of the E7 (see Note S3 and Figure S3). In addition, the response time of the E7 film from a bright to dark optical appearance decreased with an increase in the concentration of $ssRNA_{CoV}$, as shown in Figure 3E.

Our polarized light microscopy imaging revealed that the adsorption of $ssRNA_{CoV}$ caused a LC reorientation from tilted/planar to homeotropic at the DTAB-decorated aqueous-E7 interface. We notice here that our results shown in Figure 3C are strikingly similar to past studies of the DNA hybridization at an aqueous-LC interface, where hybridization between a $ssDNA_{probe}$ and a complementary targeted ssDNA caused a transition from a tilted/planar to a perpendicular orientation of the LCs at the cationic surfactant-decorated aqueous-LC interface.[37,40,41] Building from the previous studies of the DNA hybridization at LC surfaces, we hypothesize that, upon adsorption of complementary $ssRNA_{CoV}$ to the aqueous-E7 interface, the nucleobases of $ssRNA_{CoV}$ will bind to its complementary base of the $ssDNA_{probe}$ rather than remaining intercalated between the surfactant molecules due to the strong forces from hydrogen bonding and hydrophobic interactions involved in the process of hybridization. Once hybridized, the rigidity of the ssDNA-ssRNA complexes increase (e.g., the persistence length of the dsDNA increases by two orders of magnitude).[42,43] Such an increase in the rigidity compacts the double strands of the ssRNA-ssDNA, and the hydrophobic bases are no longer exposed. Therefore, the rigid ssDNA-ssRNA complexes allow for a more efficient packing at the DTAB-decorated aqueous-E7 interface and thus reorganize the DTAB to the original surface coverage prior to the $ssDNA_{probe}$ adsorption. This increase in effective surface coverage of DTAB gives rise to the transition from the planar/tilted orientation to the homeotropic orientation that is observed in our experiments.

Next, we performed two additional experiments to provide insight into the role of the target ssRNA on the ordering transition in LC films. First, we adsorbed pre-hybridized $ssDNA_{probe}$-$ssRNA_{CoV}$ to the DTAB-decorated E7 films that were prepared as described earlier (see Note S4). At concentrations up to 100 nM, the presence of pre-hybridized $ssDNA_{probe}$-$ssRNA_{CoV}$ had no measurable impact on the optical appearance of the E7 film (Figure S4). Second, we adsorbed complementary 15-mer SARS-CoV-2 ssDNA ($ssDNA_{CoV}$) (5′-CTCATCAGGAGATGC-3′) to the $ssDNA_{probe}$/DTAB-decorated aqueous-E7 interface. Similar to the $ssRNA_{CoV}$, we

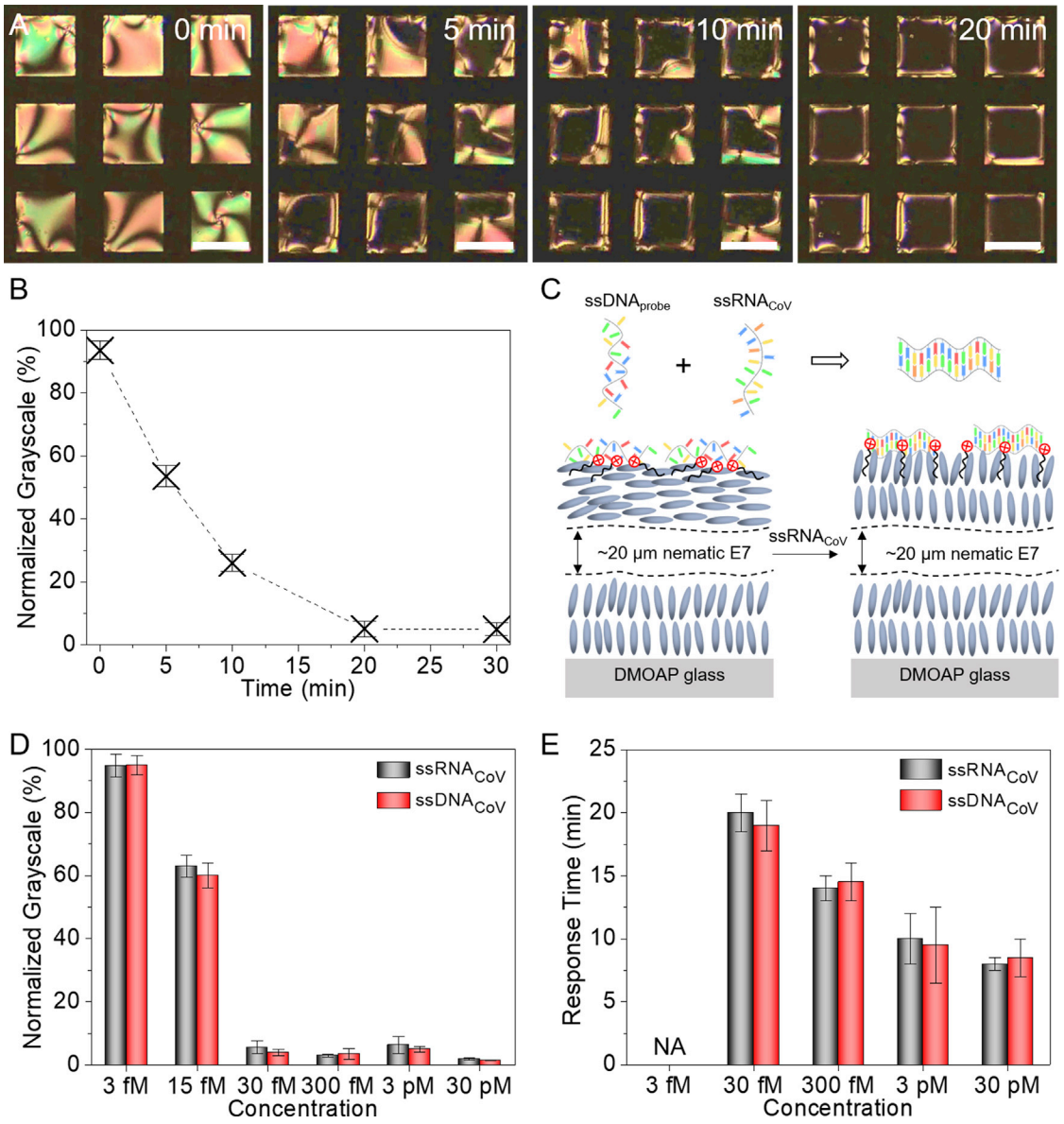

Figure 3. Adsorption of the SARS-CoV-2 RNA at the Aqueous-LC Interface

(A) Optical micrographs (crossed polarizers) of the dynamic response of the DTAB/ssDNA$_{probe}$-decorated E7 film to the adsorption of ssRNA$_{CoV}$. Scale bars, 100 μm.

(B) Normalized grayscale of the E7 films upon adsorption of ssRNA$_{CoV}$ as a function of time.

(C) Schematic illustration of the optical response of the DTAB/ssDNA$_{probe}$-decorated LC film to the adsorption of ssRNA$_{CoV}$.

(D and E) Normalized grayscale and response time of the DTAB/ssDNA$_{probe}$-decorated E7 films as a function of the concentration of ssRNA$_{CoV}$ and ssDNA$_{CoV}$. The error bars are represented as mean of three separate measurements.

observed the ssDNA$_{CoV}$ was able to trigger the ordering transition of the DTAB-decorated E7 film at remarkably low concentrations (<10^2 fM). We note here that the sensitivity of our DTAB-decorated E7 film (30 fM) is around three orders of magnitude higher than previous study on the detection of a ssDNA using a DTAB-decorated nematic LC film (50 pM).[41] The ultrasensitivity of our LC films can be attributed to the minimum surface coverage of DTAB at the aqueous-E7 interface (0.5 mM) compared with the concentration of DTAB (several mM) in the previous study.[41]

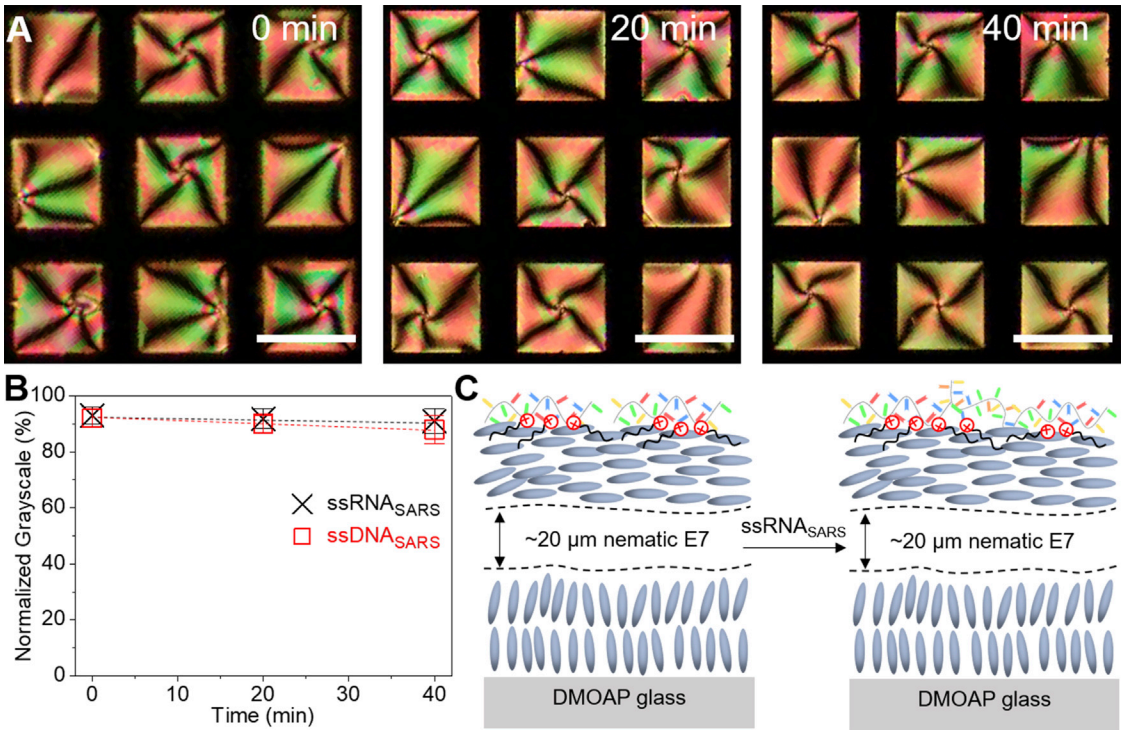

Figure 4. Adsorption of the SARS RNA at the Aqueous-LC Interface

(A) Optical micrographs (crossed polarizers) of the dynamic response of the DTAB/ssDNA$_{probe}$-decorated E7 film to the adsorption of ssRNA$_{SARS}$. Scale bars, 100 μm.

(B) Normalized grayscale of the E7 films upon adsorption of ssRNA$_{SARS}$ and ssDNA$_{SARS}$ as a function of time.

(C) Schematic illustration of the optical response of the DTAB/ssDNA$_{probe}$-decorated LC film to the adsorption of ssRNA$_{SARS}$. The error bars are represented as mean of three separate measurements.

Selectivity of LC Films

To examine the selectivity of the obtained ssDNA$_{probe}$/DTAB-decorated E7 films, 15-mer ssRNAs or ssDNAs with different degrees of base pair mismatch were tested. The first oligonucleotide sequence tested was the SARS virus, a close member of the coronavirus family that emerged in 2003, with a nucleotide sequence 5′-AUC AUCCGGUGAUGC-3′ (ssRNA$_{SARS}$), which contains a 3-bp mismatch compared with the ssDNA$_{probe}$. As shown in Figure 4A, for concentrations up to 30 nM, we measured no change in the optical appearance of the ssDNA$_{probe}$/DTAB-decorated E7 films for 90 min upon adsorption of ssRNA$_{SARS}$ (Video S2). When the concentration of ssRNA$_{SARS}$ reached 100 nM, the E7 film underwent an optical change from bright to dark after 90 min, corresponding to an ordering transition of E7 from planar/tilted to perpendicular at the aqueous-E7 interface. Moreover, we observed similar results using ssDNA$_{SARS}$ (Figure 4B). This pronounced difference in threshold concentration of ssRNA$_{CoV}$ (30 fM) and ssRNA$_{SARS}$ (100 nM) required to trigger ordering transitions within E7 films (seven orders of magnitude) leads us to hypothesis that lack of hybridization between the ssDNA$_{probe}$ and ssRNA$_{SARS}$, due to the 3-bp mismatch, caused no increase in the effective surface coverage of DTAB to trigger the E7 ordering transition at the aqueous-E7 interface (Figure 4C). We notice here that 10 μL of 30 fM ssRNA$_{CoV}$ corresponds to ~1.8×10^5 copies, which is comparable with the SARS-CoV-2 virus RNA copy number in real patient swab sample.[6]

To further test this hypothesis, we performed measurements with two additional 15-mer ssDNA sequences with different degrees of base pair mismatch: 7-bp mismatch

ssDNA ($ssDNA_{7bpm}$) (5′-AGCGTCCGGTGACGT-3′) and 15-bp mismatch ssDNA ($ssDNA_{15bpm}$) (5′-AGACGACTTCTCGTA-3′). When the ssDNA concentration reached 100 nM, the $ssDNA_{7bpm}$ triggered the optical change of the $ssDNA_{probe}$/DTAB-decorated E7 films after a period of 90 min, which is similar to the behavior of both $ssDNA_{SARS}$ and $ssRNA_{SARS}$. Additionally, the $ssDNA_{15bpm}$ failed to cause any measurable difference in the optical appearance of the E7 films over a wide concentration range (3 fM–100 nM) after 90 min. Overall, these results support our hypothesis that the response of the $ssDNA_{probe}$/DTAB-decorated LC film strongly depends on the targeted oligonucleotide sequence, which gives rise to an ultrahigh selectivity to complementary $ssRNA_{CoV}$.

Design of SARS-CoV-2 Detection Kit

In the final set of experiments for this study, we sought to design a point-of-care detection kit for SARS-CoV-2 that is visible to the human eye. We fabricated a 2.5 × 2.5 cm optical cell-based detection kit by pairing one bare glass slide and one DMOAP-functionalized glass slide each with a polarizer sheet. The two surfaces were then spaced apart with a 2-mm-thick poly(dimethylsiloxane) (PDMS) spacer, as shown in Figures 5A and 5B. An opening was conserved in the center and at one side of the PDMS spacer to allow for the analysis and the injection of the test samples, respectively. A copper specimen grid (transmission electron microscopy [TEM] grid) was placed on the surface of the DMOAP-functionalized glass slide and was subsequently filled with E7. The optical cell was then filled with a 5 mM NaCl aqueous solution containing the $ssDNA_{probe}$ at a concentration of 100 nM. We notice here that TEM grid can stabilize LC film against dewetting by water, and our LC sensors exhibit good stability under water for at least 10 days. We also comment here that this LC detection kit is not reusable. The bright optical appearance was visible to the human eye. Subsequently, 2 μL of $ssRNA_{CoV}$ or $ssRNA_{SARS}$ was added to the detection kit. When viewed with natural (sunlight) or artificial (lamp) light, a significant decrease in the brightness of the specimen grid was observed upon the addition of a 30-fM $ssRNA_{CoV}$ solution (Figure 5C) and no measurable difference in the optical appearance in the case of a 30-fM $ssRNA_{SARS}$ aqueous solution (Figure 5D).

For most real-world applications, people may visualize the result of the detection kit either under different environmental illumination conditions or at different distances, resulting in uncertainty or even error in the test result readout. To address this limitation/challenge, we employed machine learning strategy to develop a smartphone app to provide a reliable readout of the test result of our LC-based SARS-CoV-2 detection kit. The objective of this app is to provide deterministic readings for non-expert users with no background knowledge in LC sensors by utilizing the capacity of machine learning models to encode the sophisticated and non-linear visual patterns for prediction. Specifically, we employed a support vector machine (SVM),[44] which is a supervised machine learning model that is often used for statistical classification wherein the goal is to identify to which category (in this case either ''positive'' or ''negative'') a new observation belongs. Because observations are in the forms of images, a feature extraction method was designed to reduce the dimensionality of the input space. In particular, this method involves two main steps: (1) a template-matching algorithm[45] for locating the E7-infused grid and (2) the calculation of a reduced number of descriptions in terms of the standard deviation of the color value of each pixel (in Commission internationale de l'éclairage 1976 L*a*b* [CIELAB] color space) in a subdivided grid of the region of interest (see Note S5 and Figures S5–S10). The model was trained on a dataset of 88 images, with 29 positive examples and a variety of negative examples. The system is able to accurately

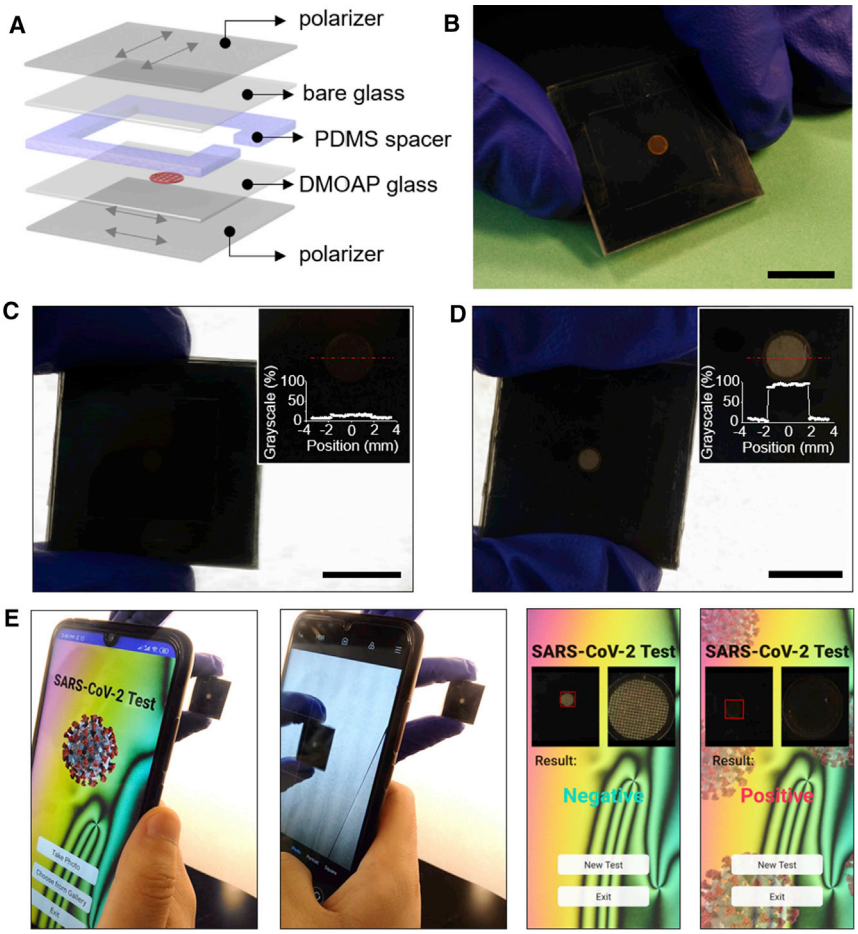

Figure 5. LC-Based Naked-Eye Home Detection Kit for SARS-CoV-2

(A and B) Design and photograph of a LC-based detection kit for $ssRNA_{CoV}$.

(C and D) Optical appearance of the LC-based detection kit when viewed under a lamp upon addition of (C) 30 fM $ssRNA_{CoV}$ and (D) 30 fM $ssRNA_{SARS}$. Scale bars, 1 cm. Insets show the normalized grayscales of the TEM grids upon the adsorption of $ssRNA_{CoV}$.

(E) Test result readout by smartphone app for negative (upon adsorption of <100 nM $ssRNA_{SARS}$) and positive (upon adsorption of >30 fM $ssRNA_{CoV}$) test results.

distinguish between the positive and negative samples given an image of the E7-infused grid (Figure 5E; Video S3). Overall, these results unmask the ways by which the $ssDNA_{probe}$ and complementary $ssRNA_{CoV}$ can be coupled at a cationic surfactant-decorated aqueous-LC interface and hint at design principles by which the nucleotide sequence of pathogenic virus RNA can be rapidly and reliably sensed using LCs.

In conclusion, it was observed that the LC ordering transitions can be triggered by adsorbing $ssRNA_{CoV}$ at a cationic surfactant/$ssDNA_{probe}$ aqueous-LC interface in a manner that depends strongly on the targeted nucleotide sequence. Additionally, when the surface coverage of DTAB was near the minimum required for a homeotropic orientation of the LCs, the minimum concentration of $ssRNA_{CoV}$ that can drive the ordering transitions in the E7 film are seven orders of magnitude lower than that of $ssRNA_{SARS}$. In comparison with conventional detection techniques, we find that $ssRNA_{CoV}$-driven ordering transitions in LC films exhibited ultrahigh sensitivity and selectivity. To the best of our knowledge, this is the first experimental evidence

that LC films can optically respond to adsorbed RNA on an interface. Our results suggest new principles for the naked-eye self-detection of viruses, including SARS-CoV-2, without requiring complex equipment or procedure.

In future work, we will investigate the selective LC detection on different SARS-CoV-2 genome sequences and similar control sequences with fewer base pair mismatches. Additionally, the massive detection of full-length SARS-CoV-2-RNA-containing patient samples will be performed in a biosafety level 3 (BSL-3) laboratory to validate its reliability. Moreover, the influence of the target ssRNA on the ordering transition of LC confined in droplets is being investigated. Future efforts will also seek to explore more sophisticated deep-learning methods for image analysis, such as convolutional neural networks (CNNs),[46] which have been successfully applied in LC chemical sensors,[47,48] semiconductors,[49] and a variety of image-based medical diagnostic tests,[50] including X-rays, ultrasounds, and magnetic resonance imaging (MRI). The main advantage of CNNs is their inherent capability to learn more complex features directly from raw data—mitigating the need to use expert knowledge to define specific hand-crafted features as done as a proof of concept in this work.

EXPERIMENTAL PROCEDURES

Resource Availability

Lead Contact

Further information should be directed to and will be fulfilled by the lead contact, Xiaoguang Wang (email: wang.12206@osu.edu).

Materials Availability

This study did not generate new unique materials.

Data and Code Availability

Further requests for datasets and code should be directed to and will be fulfilled by the Lead Contact.

Materials

Thermotropic LC E7 was purchased from Jiangsu Hecheng Advanced Materials. DTAB, DMOAP (42 wt % in methanol), NaCl, and the 15-mer ssRNA sequences (SARS-CoV-2 RNA 5′-CUCAUCAGGAGAUGC-3′; 3-bp mismatch SARS RNA 5′-AUCAUCCGGUGAUGC-3′) and 15-mer ssDNA sequences (probe DNA 5′-GCATCTCCTGATGAG-3′, complementary SARS-CoV-2 DNA 5′-CTCATCAGGAGATGC-3′, 3-bp mismatch SARS DNA 5′-ATCATCCGGTGATGC-3′, 7-bp mismatch DNA 5′-AGCGTCCGGTGACGT-3′, and 15-bp mismatch DNA 5′-AGACGACTTCTCGTA-3′) were purchased from Sigma-Aldrich. Anhydrous ethanol was obtained from Decon Labs. Microscope slides (25 × 75 × 1 mm) were purchased from Fisher Scientific. Linear polarizer sheets were obtained from Thorlabs. Copper specimen grids (GG-200Cu; 3.05 mm in diameter and 20 μm thick) were purchased from Electron Microscopy Sciences. 8-chambered cover glass system was obtained from Cellvis. Sylgard 184 PDMS precursor and curing agent were purchased from Dow Corning. Water used in all experiments was purified using a Milli-Q water purification system (Simplicity C9210). Unless stated otherwise, purchased chemicals were used as received without further modification or purification.

Preparation of DMOAP-Functionalized Glass Substrates

Glass slides were washed with water and ethanol and then dried under stream of nitrogen gas. The DMOAP aqueous solution was prepared by dissolving 1.5 wt % of DMOAP in water. The washed glass slides were placed in the DMOAP aqueous

solution and were kept at 40°C for 30 min. Afterward, the slides were rinsed with water and ethanol three times. Finally, the DMOAP-functionalized glass slides were dried under a stream of nitrogen gas and stored in the dark for further use.

Preparation of LC-Infused Specimen Grids

A copper specimen grid was placed on the surface of a DMOAP-functionalized glass slide (7 × 7 mm). Next, 0.5 μL of E7 was placed on the specimen grid using a syringe with the excess E7 being removed with a capillary tube to obtain a uniform thin film. The obtained E7-infused specimen grid was observed under polarized light microscopy to confirm the homeotropic orientation of LC mesogens within the LC film. In this work, E7 was used due to its relatively high nematic-isotropic phase transition temperature.

Adsorption of DTAB at Aqueous-LC Interfaces

The E7-filled specimen grid on the DMOAP-functionalized glass slide was immersed into a 5 mM NaCl aqueous solution (pH ranged from 5.5 to 6.0) and was subsequently exposed to a 0.5 mM DTAB solution. The E7 mesogens adopted a perpendicular anchoring at the DTAB-laden aqueous-E7 interfaces.

Optical Microscopy Characterization of LC Interfaces

The optical appearance of the E7 film during adsorption of ssRNA/ssDNA at the aqueous-E7 interface was recorded using an Olympus BX53 polarized light microscope equipped with crossed polarizers. Images were captured using a charge-coupled device (CCD) camera.

Adsorption of Probe ssDNA

The probe ssDNA ($ssDNA_{probe}$) (15-mer-5′-GCATCTCCTGATGAG-3′) was added to the DTAB-adsorbed E7 surface, and the optical response of the E7 surface was characterized with polarized light microscopy. The surface anchoring of E7 changed from homeotropic to planar/tilted within 5 min as the concentration of the $ssDNA_{probe}$ reached 100 nM, resulting in a bright optical appearance.

Detection of the Target ssRNA/ssDNA

Here, we used SARS-CoV-2 ssRNA ($ssRNA_{CoV}$) (15-mer-5′-CUCAUCAGGAGAUGC-3′) as an example. We added $ssRNA_{CoV}$ to the DTAB-laden E7 surface with the adsorbed $ssDNA_{probe}$. The temperature of the system was increased to 48.7°C, which is the T_m of the $ssRNA_{CoV}$. A Linkam PE120 Peltier hot stage was used to control the temperature of the E7 surface during these measurements. We characterized the grayscale of the E7 film over a period of 40 min. To determine the detection limit of the E7 surface for the target ssRNA/ssDNA, we varied the concentration of the target ssRNA/ssDNA from nanomolar to femtomolar concentrations.

Characterization of the Surface Tension of DTAB-Adsorbed Aqueous-LC Interfaces

A KRÜSS DSA 100 goniometer was used to measure the surface tension of aqueous-E7 interfaces using a pendant drop method. During these measurements, E7 was pushed through a needle slowly, at 5 μL/min, to minimize the effect of the dynamic forces on the shape of the droplet. Images of the pendant E7 droplet near departure were captured and analyzed using a drop shape analyzer to estimate the surface tensions.

Quantification of the Optical Appearance of the LC Films

The optical appearance (i.e., brightness) of the RNA-adsorbed E7 films was quantified from images using ImageJ software. We set the grayscale of the E7 film upon adsorption of DTAB and the $ssDNA_{probe}$ to be G_{DTAB} and G_{probe}, respectively. Upon addition of the target DNA/RNA, the grayscale of the E7 films, G, was measured and the rescaled grayscale value was calculated as

$$Rescaled\ grayscale\ = \frac{G - G_{DTAB}}{G_{probe} - G_{DTAB}} \quad \text{(Equation 1)}$$

Fabrication of Detection Kit for SARS-CoV-2

A 2.5 × 2.5 cm optical cell-based detection kit was fabricated by combining one bare glass slide and one DMOAP-functionalized glass slide each with a polarizer sheet. These combined surfaces were then spaced apart using a 2-mm-thick PDMS spacer. An opening was conserved in the center and on one side of PDMS spacer to allow for the analysis and injection of test samples, respectively. A copper specimen grid was placed on the surface of the DMOAP-functionalized glass slide and was subsequently filled with E7.

Development of a Machine-Learning-Based, Smartphone-Based App for the Detection Kit

This app takes smartphone pictures of the LC-based detection kits and provides a test result about the SARS-CoV-2 virus. The algorithm first detects the LC-infused specimen grid location from the images using a multi-scale template-matching algorithm, which can be written as

$$\arg\min_{\Omega \in K,\ s} \int_{\Omega, s} \left| J(\boldsymbol{p}) - \Psi\left(I(\boldsymbol{p})\right) \right|^2 d\boldsymbol{p}, \quad \text{(Equation 2)}$$

where K is the full smartphone image space, I refers to a specific smartphone image, s refers to the scale of the template to accommodate smartphone images taken at different distance to the image, and Ω is a subset of the image space, which is parameterized by its location and shape. J is a template of the LC-infused specimen grid at a normalized size, and Ψ refers to a brightness invariant transformation to allow the LC-infused specimen grid location algorithm to operate on image under different lighting conditions. Here, we used the well-known Canny edge operator for Ψ.[51]

In a second step, we resized the detected LC film location Ω from the smartphone images to 128 × 128 pixels and subdivided them into 4 × 4 grids, with each grid having a size of 16 × 16 pixels (each pixel has three color channels). To allow robust feature extraction, we converted the red-green-blue (RGB) images to a more computationally friend color space called CIELAB space,[52] as it separates the illumination and chromatic components well. The variances of the pixel colors within each of the LC film were concatenated as a 48-dimensional feature vector (4 × 4 grids × 3 color channels), with each component normalized between 0 and 1. The support vector machine classifier[44] was trained on the 88 independent LC detection kit samples to classify the positive and negative samples based on the extracted variance vector.

SUPPLEMENTAL INFORMATION

Supplemental Information can be found online at https://doi.org/10.1016/j.xcrp.2020.100276.

ACKNOWLEDGMENTS

J.A.P. and X.W. thank the funding support from the startup funds of The Ohio State University (OSU), and X.W. thanks OSU Institute for Materials Research Kickstart Facility Grant. X.B. thanks the funding support from the startup funds of Davidson School of Chemical Engineering at Purdue University. S.S. and R.Q. thank the funding support from Office of Naval Research (ONR grant N00014-17-1-2928).

AUTHOR CONTRIBUTIONS

The experimental strategy was proposed initially by X.B. and X.W. and developed by all authors. Y.X., A.M.R., and J.-C.F. prepared the LC surface, performed material characterization, fabricated the LC detection kit, and collected the data. Y.X., A.M.R., J.-C.F., J.A.P., X.B., and X.W. co-analyzed the experimental data. S.S., J.A.P., and R.Q. discussed the machine learning ideas, and S.S. and R.Q. developed the smartphone app. All authors discussed the results and contributed to the final manuscript, and X.W. supervised the project.

DECLARATION OF INTERESTS

The Ohio State University has filed a patent application (application number 63066000) on the work described in this manuscript. The inventors listed on the patent application are X.W., X.B., R.Q., Y.X., and A.M.R. The authors declare no other competing interests.

Received: August 24, 2020
Revised: October 1, 2020
Accepted: November 6, 2020
Published: November 17, 2020

REFERENCES

1. Chan, J.F.-W., Yuan, S., Kok, K.-H., To, K.K.-W., Chu, H., Yang, J., Xing, F., Liu, J., Yip, C.C.-Y., Poon, R.W.-S., et al. (2020). A familial cluster of pneumonia associated with the 2019 novel coronavirus indicating person-to-person transmission: a study of a family cluster. Lancet *395*, 514–523.

2. Huang, C., Wang, Y., Li, X., Ren, L., Zhao, J., Hu, Y., Zhang, L., Fan, G., Xu, J., Gu, X., et al. (2020). Clinical features of patients infected with 2019 novel coronavirus in Wuhan, China. Lancet *395*, 497–506.

3. Li, Q., Guan, X., Wu, P., Wang, X., Zhou, L., Tong, Y., Ren, R., Leung, K.S.M., Lau, E.H.Y., Wong, J.Y., et al. (2020). Early transmission dynamics in Wuhan, China, of novel coronavirus-infected pneumonia. N. Engl. J. Med. *382*, 1199–1207.

4. Zhu, N., Zhang, D., Wang, W., Li, X., Yang, B., Song, J., Zhao, X., Huang, B., Shi, W., Lu, R., et al.; China Novel Coronavirus Investigating and Research Team (2020). A novel coronavirus from patients with pneumonia in China, 2019. N. Engl. J. Med. *382*, 727–733.

5. Rothan, H.A., and Byrareddy, S.N. (2020). The epidemiology and pathogenesis of coronavirus disease (COVID-19) outbreak. J. Autoimmun. *109*, 102433.

6. Wölfel, R., Corman, V.M., Guggemos, W., Seilmaier, M., Zange, S., Müller, M.A., Niemeyer, D., Jones, T.C., Vollmar, P., Rothe, C., et al. (2020). Virological assessment of hospitalized patients with COVID-2019. Nature *581*, 465–469.

7. He, X., Lau, E.H.Y., Wu, P., Deng, X., Wang, J., Hao, X., Lau, Y.C., Wong, J.Y., Guan, Y., Tan, X., et al. (2020). Temporal dynamics in viral shedding and transmissibility of COVID-19. Nat. Med. *26*, 672–675.

8. Wang, H., Li, X., Li, T., Zhang, S., Wang, L., Wu, X., and Liu, J. (2020). The genetic sequence, origin, and diagnosis of SARS-CoV-2. Eur. J. Clin. Microbiol. Infect. Dis. *39*, 1629–1635.

9. Centers for Disease Control and Prevention (2020). Real-time RT-PCR panel for detection 2019-nCoV. https://www.cdc.gov/coronavirus/2019-ncov/lab/rt-pcr-detection-instructions.html.

10. Yuan, X., Yang, C., He, Q., Chen, J., Yu, D., Li, J., Zhai, S., Qin, Z., Du, K., Chu, Z., and Qin, P. (2020). Current and perspective diagnostic techniques for COVID-19. ACS Infect. Dis. *6*, 1998–2016.

11. Esbin, M.N., Whitney, O.N., Chong, S., Maurer, A., Darzacq, X., and Tjian, R. (2020). Overcoming the bottleneck to widespread testing: a rapid review of nucleic acid testing approaches for COVID-19 detection. RNA *26*, 771–783.

12. Yan, C., Cui, J., Huang, L., Du, B., Chen, L., Xue, G., Li, S., Zhang, W., Zhao, L., Sun, Y., et al. (2020). Rapid and visual detection of 2019 novel coronavirus (SARS-CoV-2) by a reverse transcription loop-mediated isothermal amplification assay. Clin. Microbiol. Infect. *26*, 773–779.

13. Broughton, J.P., Deng, X., Yu, G., Fasching, C.L., Servellita, V., Singh, J., Miao, X., Streithorst, J.A., Granados, A., Sotomayor-Gonzalez, A., et al. (2020). CRISPR-Cas12-based detection of SARS-CoV-2. Nat. Biotechnol. *38*, 870–874.

14. Moitra, P., Alafeef, M., Dighe, K., Frieman, M.B., and Pan, D. (2020). Selective naked-eye detection of SARS-CoV-2 mediated by N gene targeted antisense oligonucleotide capped plasmonic nanoparticles. ACS Nano *14*, 7617–7627.

15. Seo, G., Lee, G., Kim, M.J., Baek, S.H., Choi, M., Ku, K.B., Lee, C.S., Jun, S., Park, D., Kim, H.G., et al. (2020). Rapid detection of COVID-19 causative virus (SARS-CoV-2) in human nasopharyngeal swab specimens using field-effect transistor-based biosensor. ACS Nano *14*, 5135–5142.

16. Qiu, G., Gai, Z., Tao, Y., Schmitt, J., Kullak-Ublick, G.A., and Wang, J. (2020). Dual-functional plasmonic photothermal biosensors for highly accurate severe acute respiratory syndrome coronavirus 2 detection. ACS Nano *14*, 5268–5277.

17. Alves, D., Curvello, R., Henderson, E., Kesarwani, V., Walker, J.A., Leguizamon, S.C., McLiesh, H., Raghuwanshi, V.S., Samadian, H., Wood, E.M., et al. (2020). Rapid gel card agglutination assays for serological analysis following SARS-CoV-2 infection in humans. ACS Sens. *5*, 2596–2603.

18. Kléman, M., and Lavrentovich, O.D. (2003). Soft Matter Physics: An Introduction (Springer).

19. Schenning, A., Crawford, G.P., and Broer, D.J. (2018). Liquid Crystal Sensors (CRC).

20. Rasing, T.h., and Musevic, I. (2004). Surfaces and Interfaces Liquid Crystals (Springer).

21. Concellón, A., Zentner, C.A., and Swager, T.M. (2019). Dynamic complex liquid crystal emulsions. J. Am. Chem. Soc. *141*, 18246–18255.

22. Miller, D.S., Wang, X., Buchen, J., Lavrentovich, O.D., and Abbott, N.L. (2013). Analysis of the internal configurations of droplets of liquid crystal using flow cytometry. Anal. Chem. *85*, 10296–10303.

23. Moreno-Razo, J.A., Sambriski, E.J., Abbott, N.L., Hernández-Ortiz, J.P., and de Pablo, J.J. (2012). Liquid-crystal-mediated self-assembly at nanodroplet interfaces. Nature *485*, 86–89.

24. Zou, J., and Fang, J. (2011). Adhesive polymer-dispersed liquid crystal films. J. Mater. Chem. *21*, 9149–9153.

25. Kinsinger, M.I., Buck, M.E., Abbott, N.L., and Lynn, D.M. (2010). Immobilization of polymer-decorated liquid crystal droplets on chemically tailored surfaces. Langmuir *26*, 10234–10242.

26. Brake, J.M., Daschner, M.K., Luk, Y.Y., and Abbott, N.L. (2003). Biomolecular interactions at phospholipid-decorated surfaces of liquid crystals. Science *302*, 2094–2097.

27. Zhao, Y., Mahajan, N., Lu, R., and Fang, J. (2005). Liquid-crystal imaging of molecular-tilt ordering in self-assembled lipid tubules. Proc. Natl. Acad. Sci. USA *102*, 7438–7442.

28. Cumberland, J., Lopatkina, T., Murachver, M., Popov, P., Kenderesi, V., Buka, Á., Mann, E.K., and Jákli, A. (2018). Bending nematic liquid crystal membranes with phospholipids. Soft Matter *14*, 7003–7008.

29. Manna, U., Zayas-Gonzalez, Y.M., Carlton, R.J., Caruso, F., Abbott, N.L., and Lynn, D.M. (2013). Liquid crystal chemical sensors that cells can wear. Angew. Chem. Int. Ed. Engl. *52*, 14011–14015.

30. Wang, X., Yang, P., Mondiot, F., Li, Y., Miller, D.S., Chen, Z., and Abbott, N.L. (2015). Interfacial ordering of thermotropic liquid crystals triggered by the secondary structures of oligopeptides. Chem. Commun. (Camb.) *51*, 16844–16847.

31. Hartono, D., Xue, C.-Y., Yang, K.-L., and Yung, L.-Y.L. (2009). Decorating liquid crystal surfaces with proteins for real-time detection of specific protein-protein binding. Adv. Funct. Mater. *19*, 3574–3579.

32. Zhu, Q., and Yang, K.-L. (2013). Amplification of interference color by using liquid crystal for protein detection. Appl. Phys. Lett. *103*, 243701.

33. Zhang, W., Ang, W.T., Xue, C.Y., and Yang, K.L. (2011). Minimizing nonspecific protein adsorption in liquid crystal immunoassays by using surfactants. ACS Appl. Mater. Interfaces *3*, 3496–3500.

34. Daschner De Tercero, M., and Abbott, N.L. (2008). Ordering transitions in liquid crystals permit imaging of spatial and temporal patterns formed by proteins penetrating into lipid-laden interfaces. Chem. Eng. Commun. *196*, 234–251.

35. Eimura, H., Miller, D.S., Wang, X., Abbott, N.L., and Kato, T. (2016). Self-assembly of bioconjugated amphiphilic mesogens having specific binding moieties at aqueous–liquid crystal interfaces. Chem. Mater. *28*, 1170–1178.

36. Lin, I.H., Miller, D.S., Bertics, P.J., Murphy, C.J., de Pablo, J.J., and Abbott, N.L. (2011). Endotoxin-induced structural transformations in liquid crystalline droplets. Science *332*, 1297–1300.

37. McUmber, A.C., Noonan, P.S., and Schwartz, D.K. (2012). Surfactant–DNA interactions at the liquid crystal–aqueous interface. Soft Matter *8*, 4335–4342.

38. Lai, S.L., Hartono, D., and Yang, K.-L. (2009). Self-assembly of cholesterol DNA at liquid crystal/aqueous interface and its application for DNA detection. Appl. Phys. Lett. *95*, 153702.

39. Zhou, J., Dong, Y., Zhang, Y., Liu, D., and Yang, Z. (2016). The assembly of DNA amphiphiles at liquid crystal-aqueous interface. Nanomaterials (Basel) *6*, 229–238.

40. Price, A.D., and Schwartz, D.K. (2008). DNA hybridization-induced reorientation of liquid crystal anchoring at the nematic liquid crystal/aqueous interface. J. Am. Chem. Soc. *130*, 8188–8194.

41. Khan, M., Khan, A.R., Shin, J.H., and Park, S.Y. (2016). A liquid-crystal-based DNA biosensor for pathogen detection. Sci. Rep. *6*, 22676.

42. Cui, S., Yu, Y., and Lin, Z. (2009). Modeling single chain elasticity of single-stranded DNA: A comparison of three models. Polymer *50*, 930–935.

43. Mandelkern, M., Elias, J.G., Eden, D., and Crothers, D.M. (1981). The dimensions of DNA in solution. J. Mol. Biol. *152*, 153–161.

44. Wang, L. (2005). Support Vector Machines: Theory and Applications (Springer).

45. Atallah, M.J. (2001). Faster image template matching in the sum of the absolute value of differences measure. IEEE Trans. Image Process. *10*, 659–663.

46. Lo, S.-C.B., Chan, H.-P., Lin, J.-S., Li, H., Freedman, M.T., and Mun, S.K. (1995). Artificial convolution neural network for medical image pattern recognition. Neural Netw. *8*, 1201–1214.

47. Cao, Y., Yu, H., Abbott, N.L., and Zavala, V.M. (2018). Machine learning algorithms for liquid crystal-based sensors. ACS Sens. *3*, 2237–2245.

48. Smith, A.D., Abbott, N., and Zavala, V.M. (2020). Convolutional network analysis of optical micrographs for liquid crystal sensors. J. Phys. Chem. C *124*, 15152–15161.

49. O'Leary, J., Sawlani, K., and Mesbah, A. (2020). Deep learning for classification of the chemical composition of particle defects on semiconductor wafers. IEEE Trans. Semicond. Manuf. *33*, 72–85.

50. Anwar, S.M., Majid, M., Qayyum, A., Awais, M., Alnowami, M., and Khan, M.K. (2018). Medical image analysis using convolutional neural networks: a review. J. Med. Syst. *42*, 226.

51. Canny, J. (1986). A computational approach to edge detection. IEEE Trans. Pattern Anal. Mach. Intell. *8*, 679–698.

52. Joblove, G.H., and Greenberg, D. (1978). Color spaces for computer graphics. Comput. Graph. *12*, 20–25.

Cell Reports Physical Science, Volume *1*

Supplemental Information

Ultrasensitive and Selective Detection of SARS-CoV-2 Using Thermotropic Liquid Crystals and Image-Based Machine Learning

Yang Xu, Adil M. Rather, Shuang Song, Jen-Chun Fang, Robert L. Dupont, Ufuoma I. Kara, Yun Chang, Joel A. Paulson, Rongjun Qin, Xiaoping Bao, and Xiaoguang Wang

Note S1. Adsorption of DTAB and change in liquid crystal (LC) orientation

As described in the main text, the adsorption of DTAB on the E7 surface caused a change in the E7 orientation from planar to homeotropic while the subsequent adsorption of the $ssRNA_{probe}$ returned the orientation of E7 to a planar surface orientation. The reorientation back to a planar orientation of the E7 mesogens occurs only when the DTAB is used at an appropriate concentration coinciding with the minimum surface coverage needed for a homeotropic orientation. After various trials with varying concentrations of DTAB in the system, we found that 0.5 mM DTAB is the appropriate concentration that provides the minimum surface coverage needed, allowing for the required changes in the E7 orientation. Therefore, we selected 0.5 mM DTAB as the experimental system. In contrast, at higher DTAB concentrations, 6 mM, for example, the homeotropic orientation of E7 at the aqueous–E7 interface was unaffected by the presence of the $ssDNA_{probe}$, as shown in Figure S1.

These observations of the DTAB concentration-dependent E7 optical responses can be explained with the proposition that at low concentrations of DTAB, the $ssDNA_{probe}$ molecules are capable of introducing themselves between the DTAB molecules to readily interact with the E7 surface, while at higher DTAB concentrations, the interface is highly crowded with DTAB molecules and thus the $ssDNA_{probe}$ molecules are not able to penetrate into the layer between surfactant molecules to associate with the E7 phase. As a result, at a high DTAB concentration, the $ssDNA_{probe}$ may still bind with the surface, but no E7 reorientation would be observed (Figure S1). These results lead us to conclude that the concentration of the cationic surfactant plays a vital role in the detection of ssRNA and ssDNA molecules. Hence this experiment demonstrates the presence of an optimum concentration of DTAB needed for the detection of ssRNA and ssDNA at ultralow concentrations.

Note S2. Surface coverage of DTAB at aqueous–E7 interfaces

To provide more insights into our observation of a DTAB concentration-dependent E7 response, we performed an interfacial tension measurement between the DTAB aqueous solution and E7. The aqueous–E7 interfacial tension was measured using a pendant droplet model and the average values were calculated using 10 separate measurements from each of three different droplets. For the measurement of the aqueous–E7 interfaces in a DTAB solution, a DTAB aqueous solution was placed in a quartz cell. Next, E7 was loaded into a syringe and the tip of the needle was placed under the surface of the DTAB solution. A high-resolution camera was connected with the goniometer (KRUSS DSA 100), which was used to capture the images of the droplet. Various inputs, including density, surface tension and the volume of the droplet, were provided to the built-in software, ADVANCE, to calculate the interfacial tension. The DTAB solution was prepared in a 5 mM NaCl aqueous solution having a pH between 5.5 and 6.0 to maintain the consistency of the experimental procedure.

From our interfacial tension measurements, it was found that the interfacial tension decreases significantly with an increase in the concentration of DTAB until it reached a critical micelle concentration (CMC; approximately 14 mM at 25 ^{o}C)[1] and remained nearly constant above this concentration (Figure S2). These results lead us to conclude that a partial monolayer adsorption of DTAB was achieved on the aqueous–E7 interface at 0.5 mM DTAB and that such a concentration is sufficient enough to change the E7 orientation while allowing for the facile intercalation of the $ssDNA_{probe}$ and the $ssRNA_{CoV}$/$ssDNA_{CoV}$ target with the E7 surface, which is required for detection. To support our hypothesis, we estimated the percentage of the surface covered by the DTAB at aqueous–E7 interfaces using the following equation[2]:

$$\gamma - \gamma_{\circ} = \Gamma_{\infty} RT[\, ln\,(1 - m)] - \frac{Km^2}{2} \quad \text{S.1}$$

where R is the gas constant (8.314 J mol^{-1} K^{-1}), T is the absolute temperature, m is the fraction of surface coverage, and γ and $\gamma_{\circ}$ are the interfacial tension of the aqueous–E7 interface with and without DTAB, respectively. Γ_{∞}, which represents the maximum surface concentration for DTAB, is 3.17×10^{-3} mol/cm^2.[3] For simplicity, we set the cooperativity term $K = 0$. For concentrations up to the CMC of DTAB (approximately 14 mM), the coverage of DTAB at the aqueous–E7 interfaces increases with an increase in the concentration of DTAB, as shown in Figure S2B. When the concentration of DTAB was above the CMC, however, the surface was saturated with DTAB. We notice here that at 0.5 mM DTAB, the percentage of surface coverage is estimated to be around 36%. This calculation result supports our assumption of partial surface coverage of DTAB at 0.5 mM, and suggests that a substantial amount of the surface area at the interface is an open LC surface. We comment here that this low surface coverage of DTAB plays a critical role in ultrasensitive detection of SARS-CoV-2. In addition, we have performed additional experiments to show the effect of DTAB concentration on the sensitivity of LC sensor to SARS-CoV-2 virus. As increase in the DTAB concentration at the LC surface, the threshold concentration of SARS-CoV-2 that causes perpendicular-to-planar ordering transition of the LC increases, which is caused by the strong perpendicular anchoring of the LC at the surface (Figure S2C).

Note S3. Effect of $ssRNA_{CoV}$ on the optical appearance of the E7 film

Grayscale intensity was used to quantify the brightness change of the E7 film with the addition of the $ssDNA_{probe}$ and the target $ssRNA_{CoV}$ over time as shown in the main text. Here we performed an adsorption of 3 fM $ssRNA_{CoV}$ below the threshold concentration of the detection limit. At such low concentrations no measurable change in the brightness of the E7 film was observed after 60

minutes, as shown in Figure S3. When the concentration of $ssRNA_{CoV}$ is 30 fM or above, the grayscale of the E7 was measured to decrease with an increase in the adsorption of $ssRNA_{CoV}$ at the surface, as shown in Figures 3D and 3E of the main text. Therefore, these results lead us to conclude that the detection limit of our designed E7-based system for $ssRNA_{CoV}$ is 30 fM.

Note S4. Adsorption of prehybridized $ssDNA_{probe}$ and $ssRNA_{CoV}$

As demonstrated in the main text, the successful adsorption of the $ssDNA_{probe}$ and $ssRNA_{CoV}$ was performed discretely in two different steps. The adsorption of the $ssDNA_{probe}$ and $ssRNA_{CoV}$ is based on the electrostatic interaction and hybridization of base pairs. To provide further insight, here we studied the adsorption of prehybridized $ssDNA_{probe}$–$ssRNA_{CoV}$ on the DTAB-decorated surface. Specifically, we first mixed the $ssDNA_{probe}$ and the $ssRNA_{CoV}$ in a 5 mM NaCl aqueous solution, and subsequently added the prehybridized $ssDNA_{probe}$–$ssRNA_{CoV}$ to the DTAB-decorated E7 film. We found that, over a wide concentration range (up to 100 nM), the prehybridized $ssDNA_{probe}$–$ssRNA_{CoV}$ caused no measurable changes to the optical appearance of the E7 film, as shown in Figure S4. Hence, the designed E7-based system is applicable for the detection of $ssRNA_{CoV}$ and is inept for double stranded or prehybridized $ssDNA_{probe}$–$ssRNA_{CoV}$. These results suggest the lack of interaction between the prehybridized $ssDNA_{probe}$–$ssRNA_{CoV}$ and the DTAB-decorated aqueous–E7 interface owing to the absence of electrostatic charges on the prehybridized $ssDNA_{probe}$–$ssRNA_{CoV}$.

Note S5. Development of a machine learning-based smartphone-based application (App) for detection kit

Our recognition system was built based on 88 independent sample images collected using a smartphone. 29 samples that were exposed to $ssRNA_{CoV}$ with concentrations $\geq$ 30 fM were marked

as positive, and the rest were marked as negative and categorized as either 'exposed to SARS' or 'not exposed'. The recognition system has two modules: (1) LC area detection, which locates the LC-infused specimen grid from the images, and (2) a patch-based machine learning system for classifying the texture of LC-infused grids.

Detection of the LC-infused grid

Since the LC-based detection kit presented a regular circular shape with textures, we adopted an image template matching method to locate the desired LC-infused grid. This method operated a per-pixel type of search, which scanned over the images of the detection kit, as shown in Figure S5. This method returned a location with a maximum correlation to the template.[4] Because of the images varied in brightness due to different environmental illumination conditions, the template matching needed to operate on a transformed image which was invariant to lightness and/or brightness differences. Additionally, the images might be taken at different distances to the detection kit, resulting in scale differences. To address these challenges, we used a multi-scale template matching algorithm to determine the location of the LC-infused grid:

$$\arg\min_{\Omega \in K,s} \int_{\Omega,s} |J(\boldsymbol{p}) - \Psi(I(\boldsymbol{p}))|^2 d\boldsymbol{p} \qquad \text{S.2}$$

where K is the full smartphone image space, I refers to a specific smartphone image, s refers to the scale of the template to accommodate smartphone images taken at different distance to the image, and Ω is a subset of the image space, which is parameterized by the its location and shape. J is a template of the LC-infused specimen grid at a normalized size, and Ψ refers to a brightness invariant transformation to allow the LC-infused specimen grid location algorithm to operate on images under different lighting conditions. Here we used the well-known Canny edge operator for Ψ[5]. We note here that equation (S2) is the same as equation (2) in the main text.

The optimization of equation (S2) was performed using a regular square-based template. Specifically, the distance metric of $|J(\boldsymbol{p}) - \Psi(I(\boldsymbol{p}))|^2$ was transformed to a correlation of $J(\boldsymbol{p})$ and $\Psi\big(I(\boldsymbol{p})\big)$. Figure S6 shows the matching probability map (the matching result) of six methods provided by OpenCV.[6] In our work, we selected cross correlation (shown in Figure S6C) as the matching probability estimator, and the corresponding equation can be written as:

$$CCORR(x, y) = \sum_{x',y'} (J(x', y') \cdot \Psi(I(x + x', y + y')) \quad \text{S.3}$$

where I is an input image to be detected and $\Psi(I)$ refers to the edge transformation. *CCORR* is the probability map which is built by sliding the template over the image and computing at each location. For more details about template matching, we would refer readers to Reference 4.

Next, we took a multi-scale approach for template matching, in which an image pyramid is built on the source images.[7] As shown in Figure S7, the searching analyzes the image with different scales and locates the LC-infused grid with the best correlation to the template. In our system, we defined 20 scales on the image to cover most of the distances that a user exercises for smartphone images.

Finally, we used an edge feature of the images to address the uncertainties caused by the different brightness levels of the image due to different environmental lighting conditions. The images were transformed through a Canny edge operator,[5] which executed a series of refinements on an edge magnitude map produced through a Laplacian operator. As shown in Figure S8, with two images of significantly different illuminations, the Canny operators captured the textural properties of the visual patterns of the LC-infused grid, and thus effectively improved the accuracy of the template matching. In summary, this multi-scale template matching method succeeded at all 88 independent images in our experiments.

Below is the code for the multi-scale template matching method:

```python
import cv2 as cv
import numpy as np

def roiDetection(IMAGE_PATH,TEMPLATE_PATH,canny_param1=20,canny_param2=50):
    '''''
    IMAGE_PATH: source image path, e.g. taken by mobilephone
    TEMPLATE_PATH: template image path
    canny_param1: parameter of Canny edge operator, default 20
    canny_param2: parameter of Canny edge operator, default 50

    '''
    # Load Template, convert to gray scale and apply edge operator
    template = cv.imread(TEMPLATE_PATH)
    template = cv.cvtColor(template, cv.COLOR_BGR2GRAY)
    template = cv.Canny(template, canny_param1, canny_param2)
    tH, tW = template.shape

    # Load source image, convert to gray scale
    image = cv.cvtColor(cv.imread(IMAGE_PATH), cv.COLOR_BGR2RGB)
    gray = cv.cvtColor(image, cv.COLOR_BGR2GRAY)

    found = None

    # Loop over the scales of the source image
    for scale in np.linspace(0.5, 2.0, 20)[::-1]:
        rH = int(gray.shape[0]*scale)
        rW = int(gray.shape[1]*scale)
        # Resize the image according to the scale
        resized = cv.resize(gray, (rH, rW))

        r = gray.shape[1] / float(resized.shape[1])

        if resized.shape[0] < tH or resized.shape[1] < tW:
            break

        # Apply edge operator on source image
        edged = cv.Canny(resized, canny_param1, canny_param2)
        # Execute template matching
        result = cv.matchTemplate(edged, template, cv.TM_CCOEFF)
        (_, maxVal, _, maxLoc) = cv.minMaxLoc(result)

        # Record location, scale, and response value of matching probablity
        if found is None or maxVal > found[0]:
            found = (maxVal, maxLoc, r)

    # Get the location and scale with maximal matching probability across all scales
    (_, maxLoc, r) = found

    # Compute corresponding bounding box at scale 1.0
    (startX, startY) = (int(maxLoc[0] * r), int(maxLoc[1] * r))
    (endX, endY) = (int((maxLoc[0] + tW) * r), int((maxLoc[1] + tH) * r))

    # Crop Region of Interest from source image
    ROI_image = image[startY:endY,startX:endX,:]
    return ROI_image, (startX,startY,endX,endY)
```

Machine learning system for visual pattern recognition of the LC-infused grid

To detect the status of the LC-infused grid in the image, we designed a feature based on the textural properties and optical appearance of the LC-infused grid. This procedure consists of three steps: (1) radiometric correction for the images taken under a variety of environmental lighting conditions, (2) color transformation from RGB to a CIELAB[8] space for color distance metric computation, and (3) feature vector extraction.

Radiometric correction

To address the challenge that the images might be taken by users under different lighting conditions, we used a radiometric correction which transforms the images to be lightness-invariant. Here we used a linear model to represent the illumination by correcting the image patches with homogenous lightness over the LC-infused grid region. The linear model consists of three parameters, which form a plane in three-dimensional space, which can be written as:

$$\hat{I}_{\mathrm{x,y}} = a \cdot x + b \cdot y + c \qquad \text{S.4}$$

where a, b, c are parameters of the model, and $\hat{I}_{\mathrm{x,y}}$ is the expected pixel value at the location (x, y). The corrected pixel values then are presented by residuals from a perfect plane:

$$e_{x,y} = I_{x,y} - \hat{I}_{\mathrm{x,y}} \qquad \text{S.5}$$

in which $I_{x,y}$ is the raw pixel measurement. A representative example of an unevenly illuminated image patch is shown in Figure S9A. Inspection of Figure S9B and S9C reveals that, compared with a simple mean correction (*i.e.*, zero-mean values), the plane-based correction recovered a well-illuminated image.

Below is the code for radiometric correction:

```
import cv2 as cv
import numpy as np

def meanNormalize(input_image):
    '''''
    input image: a 3D numpy matrix with shape=(Height,Width,Channel)
                 and dtype=numpy.uint8
    '''
    # zero-mean the image by subtracting mean value
    return input_image.astype(np.float) - np.mean(np.mean(input_image,axis=0),axis=0)

def planeMeanNormalize(input_image):
    '''''
    input image: a 3D numpy matrix with shape=(Height,Width,Channel)
                 and dtype=numpy.uint8
    '''
    input_image = input_image.astype(np.float)
    output_img = input_image

    zn =  input_image.shape[2] # number of channels
    num_px = input_image.shape[0]*input_image.shape[1]

    # build linear system [ci, ri, 1] * [a, b, c]^T = Ii
    matA = np.zeros((num_px,3))
    matB = np.zeros(num_px)
    for zi in range(zn):
        for ri in range(input_image.shape[0]):
            for ci in range(input_image.shape[1]):
                pxidx = ri*input_image.shape[1]+ci
                matA[pxidx,0] = ci
                matA[pxidx,1] = ri
                matA[pxidx,2] = 1
                matB[pxidx] = input_image[ri,ci,zi]
        # Least Squared Solution
        x = np.linalg.lstsq(matA,matB)
        # Compute adjusted observation
        for ri in range(input_image.shape[0]):
            for ci in range(input_image.shape[1]):
                pxidx = ri*input_image.shape[1]+ci
                output_img[ri,ci,zi] = output_img[ri,ci,zi] - np.dot(x[0],matA[pxidx,:]
.ravel())
    return input_image
```

Conversion from RGB to a CIE Lab color space and feature vector extraction

We converted the RGB image to a CIE Lab color space, since it is known to be perceptually more meaningful for color distance computation. Subsequently, feature extraction was performed on the normalized image in the CIE Lab space. To homogenize the input for our features, we subdivided the ROI into 4 × 4 grids, from a resized 128 × 128 pixels image of the LC-infused grid, as shown in Figure S10. We used the standard deviation (std) metric within one grid to represent the homogeneity/heterogeneity of the LC-infused grid, which can be written as:

$$std = \sqrt{\frac{1}{|C|}\sum_{i \in C} e_i^2} \quad \text{S.6}$$

where C is the region of the grid, $|C|$ is the number of pixels in the grid, e_i is the pixel value at location i, which was corrected following the step described in section 5.2.1. The values from the grid ($4 \times 4 \times 3$, where "3" represents the number of image color channels) of std were concatenated into a 48×1 vector which served as the feature of the Support Vector Machine (SVM)[9] classifier.

Below is the code for feature vector extraction:

```
import cv2 as cv
import numpy as np

def extractFeature(image,W=4):
    '''''
    image: A 3D numpy matrix with shape=(Height,Width,Channel)
        and dtype=numpy.uint8
    W: output grid height and width, default 4
    '''
    # Resize input with any size to 128 x 128 x Channel
    resized = cv.resize(image, (128, 128))
    # Convert to CIELAB color space
    lab = cv.cvtColor(resized.astype(np.float32)/255.,cv.COLOR_RGB2LAB)
    # Radiometric correction with linear model
    normaized = planeMeanNormalize(lab)

    # Width of each cell of grid
    TW = int(128/W)
    C=normaized.shape[2]
    output_grid = np.zeros((W,W,C),dtype=np.float)

    # Loop over each grid cell and each channel
    for ci in range(W):
        for ri in range(W):
            block = normaized[ri*TW:(ri+1)*TW,ci*TW:(ci+1)*TW,:]
            for zi in range(C):
                # Compute standard derivation of pixels in
                std = np.sqrt(np.mean(block[:,:,zi].ravel()**2))
                output_grid[ri,ci,zi] = std
    # Convert WxWxC 3d grid to (WxWxC) x 1 vector
    featureVec = output_grid.ravel()
    return featureVec
```

App implementation

The Android smartphone App was built using Android Studio. Video S3 shows a typical use case of our application, including the start page and the test results. The operation of the App was

designed to be user friendly and robust. For example, the users can either take a picture with the camera of the mobile phone or select one from the photo gallery. The App can automatically detect the region where the LC-infused grid is located, perform the machine learning-based analysis, and then report the results.

We verified our LC-infused grid detection module and pattern recognition module in Python on the workstation. The detection module was mainly implemented based on the OpenCV library[6], which supports both low-level image processing tools as well as high-level algorithms. The SVM classifier was trained in Python using Scikit-Learn,[10] a well-known and open-source machine learning toolkit. The model was then serialized with the PMML package,[11] an exchange format which describes the predictive models. To port to the Android operating system, we located open-sourced libraries corresponding to those used in Python.

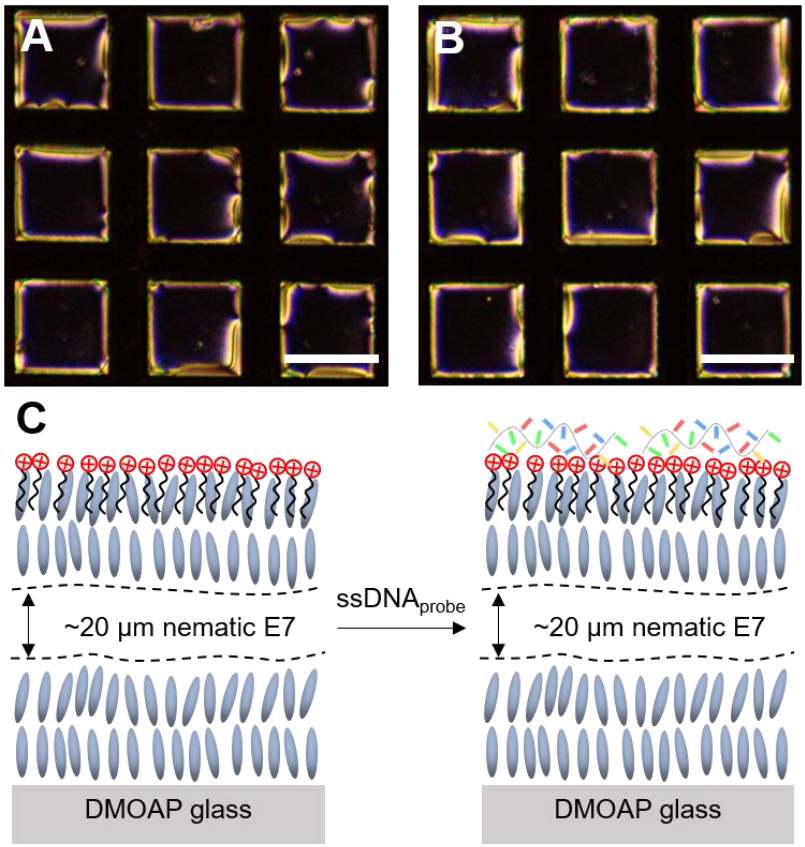

Figure S1. Adsorption of a highly concentrated solution of DTAB at the aqueous–E7 interface. (A-B) Optical micrographs (crossed polarizers) of the E7 film during (A) the adsorption of the highly concentrated solution of DTAB (6 mM) and (B) after adsorption of the ssDNA$_{probe}$. Scale bars, 100 µm. (C) Schematic illustration of the optical response of the E7 films after the adsorption of the highly concentrated solution of DTAB (6 mM) and adsorption of ssDNA$_{probe}$, respectively.

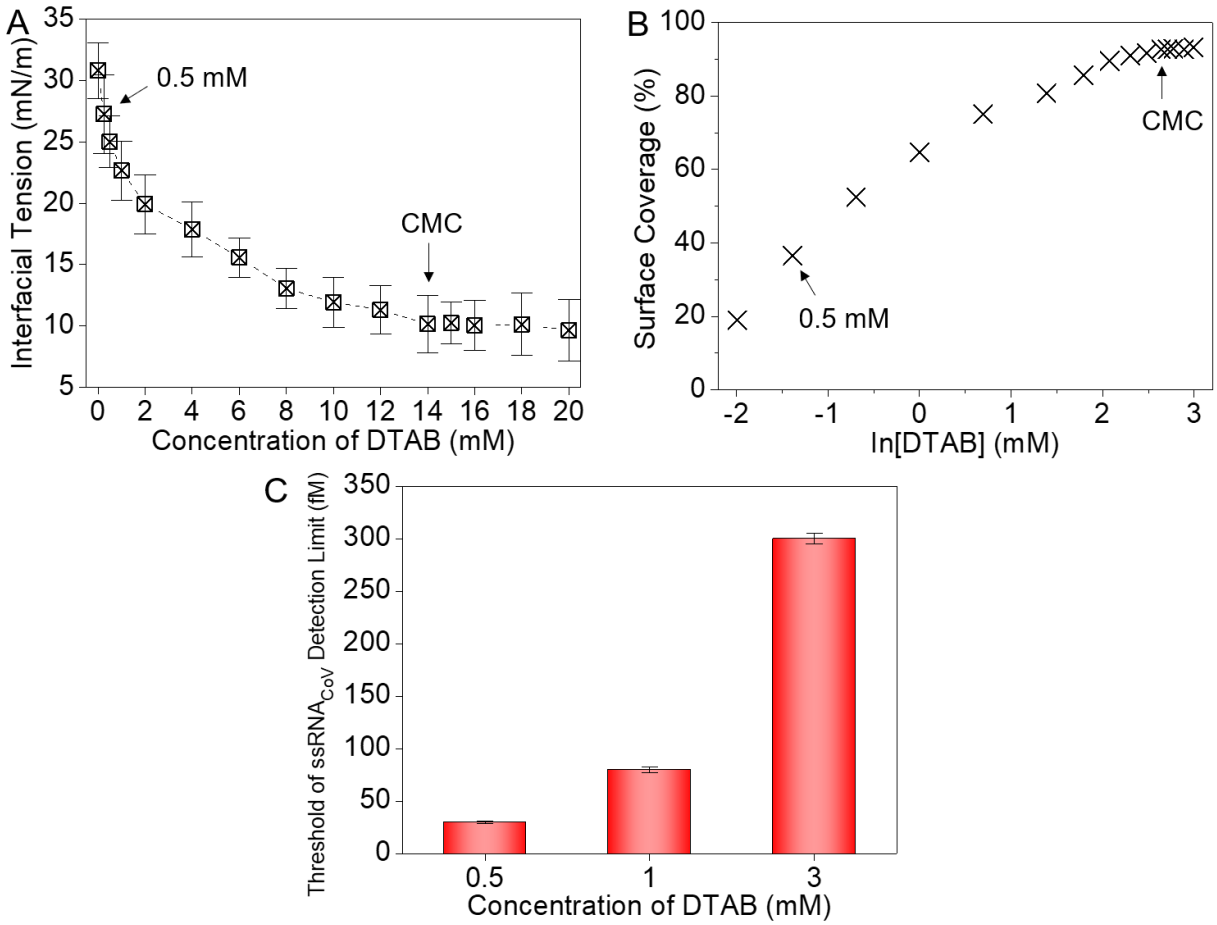

Figure S2. Surface coverage of DTAB as a function of bulk concentration. (A) Plot illustrating the change in the interfacial tension of the aqueous–E7 interface with a varying concentration of DTAB from 0 mM to 20 mM. (B) Plot of the surface coverage of DTAB at the aqueous–E7 interface as a function of the bulk concentration of DTAB in the aqueous phase. The aqueous phase contains 5 mM NaCl. The surface coverage of DTAB increases with an increase in the concentration of DTAB in the bulk aqueous phase, and remains nearly constant beyond the critical micelle concentration of DTAB. (C) Plot illustrating the threshold of SARS-CoV-2 detection limit with different DTAB concentrations. The error bars are represented as mean of three separate measurements.

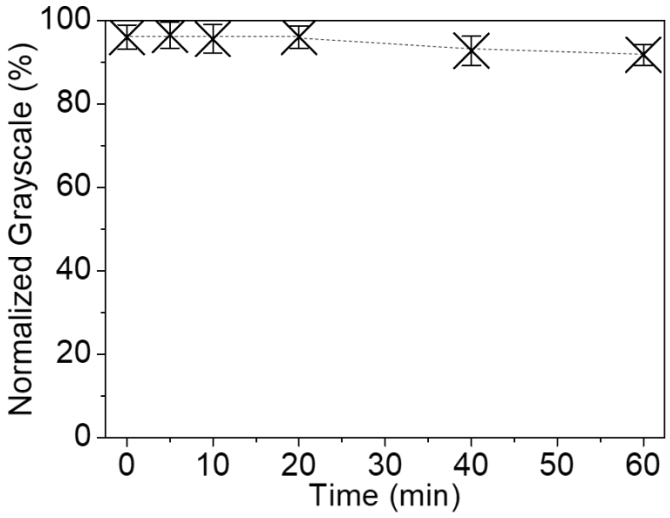

Figure S3. Plot displaying the normalized grayscale intensity of DTAB/ssDNA$_{probe}$-decorated E7 film upon adsorption of ssRNA$_{CoV}$ as a function of time. The concentration of ssRNA$_{CoV}$ is 3 fM. The error bars are represented as mean of three separate measurements.

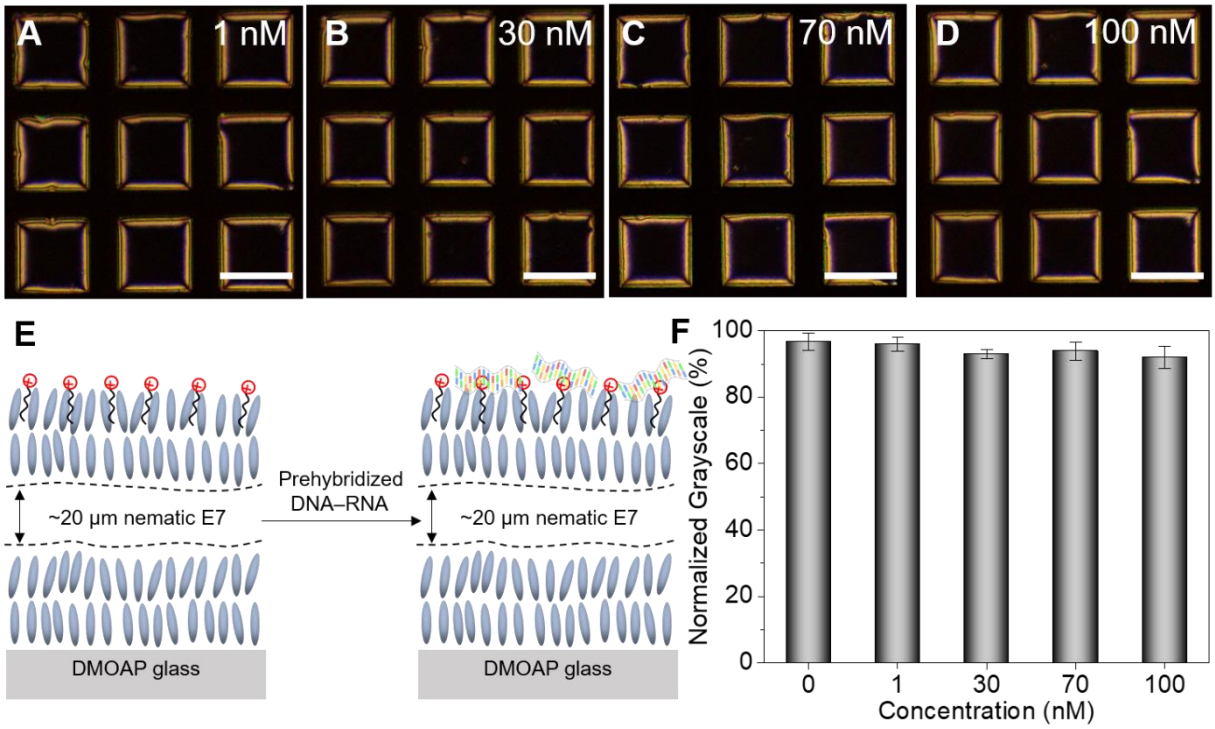

Figure S4. Adsorption of prehybridized DNA–RNA ($ssDNA_{probe}$–$ssRNA_{CoV}$) on the aqueous–E7 interface. (A-D) Optical micrographs (crossed polarizers) of the E7 film after the adsorption of prehybridized DNA with different concentrations including (A) 1 nM, (B) 30 nM, (C) 70 nM, and (D) 100 nM. Scale bars, 100 μm. (E) Schematic illustration of the optical response of the DTAB-decorated E7 film to the adsorption of prehybridized DNA. (F) Plot illustrating the normalized grayscale intensity of the DTAB-decorated E7 films with different concentrations of prehybridized $ssDNA_{probe}$–$ssRNA_{CoV}$. The error bars are represented as mean of three separate measurements.

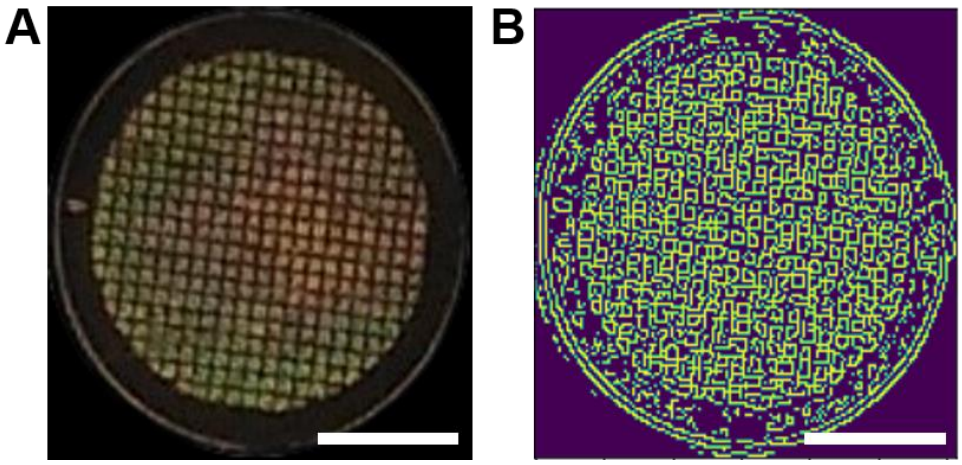

Figure S5. Image template of LC-infused grid. (A) RGB image of the template, consisting of 3 channels. (B) A single band image with the brightness invariant feature of the template extracted by Canny edge operator. Scale bars, 1 mm.

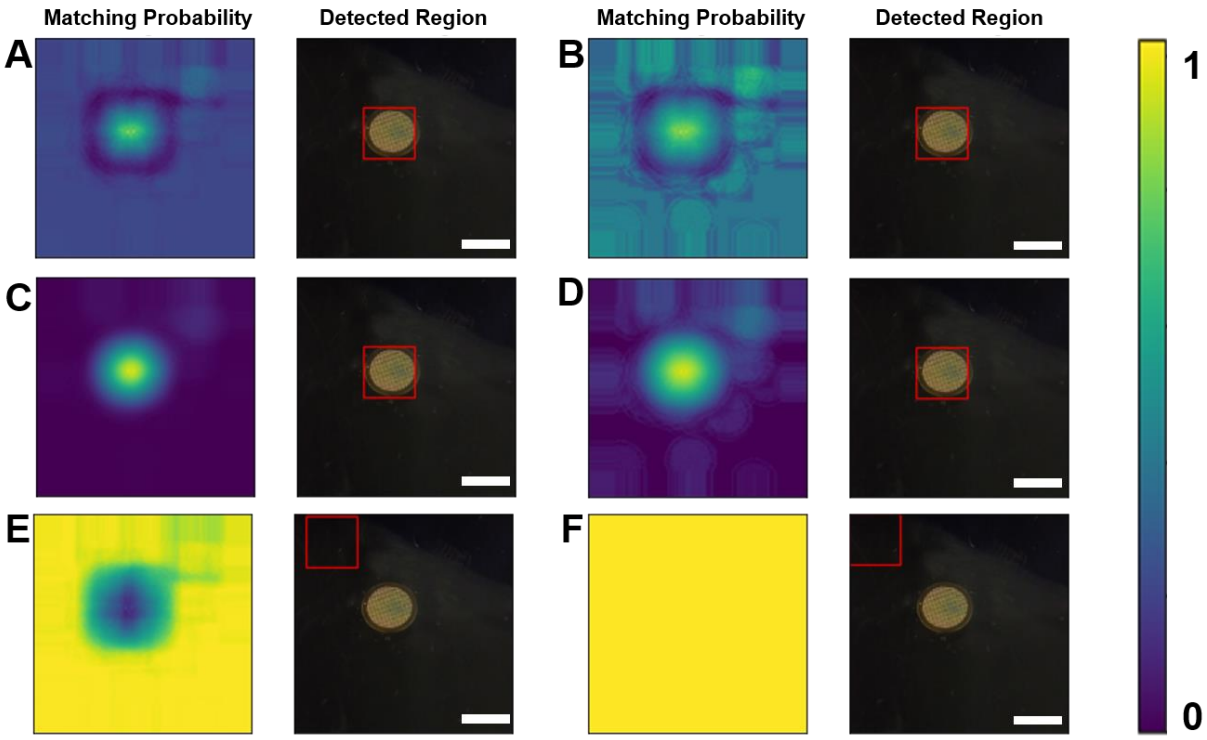

Figure S6. Performance evaluation of different template matching metrics. (A-F) Matching probability and detection regions of (A) Correlation Coefficient, (B) Normalized Correlation Coefficient, (C) Cross Correlation, (D) Normalized Cross Correlation, (E) Squared Distance and (F) Normalized Squared Distance. The red box in the right side of each panel shows the location with highest matching probability. In our work, we selected (C) Cross Correlation as the matching metric due to the best distribution of the matching probability. Scale bars, 3 mm. The color bar represents the matching probability.

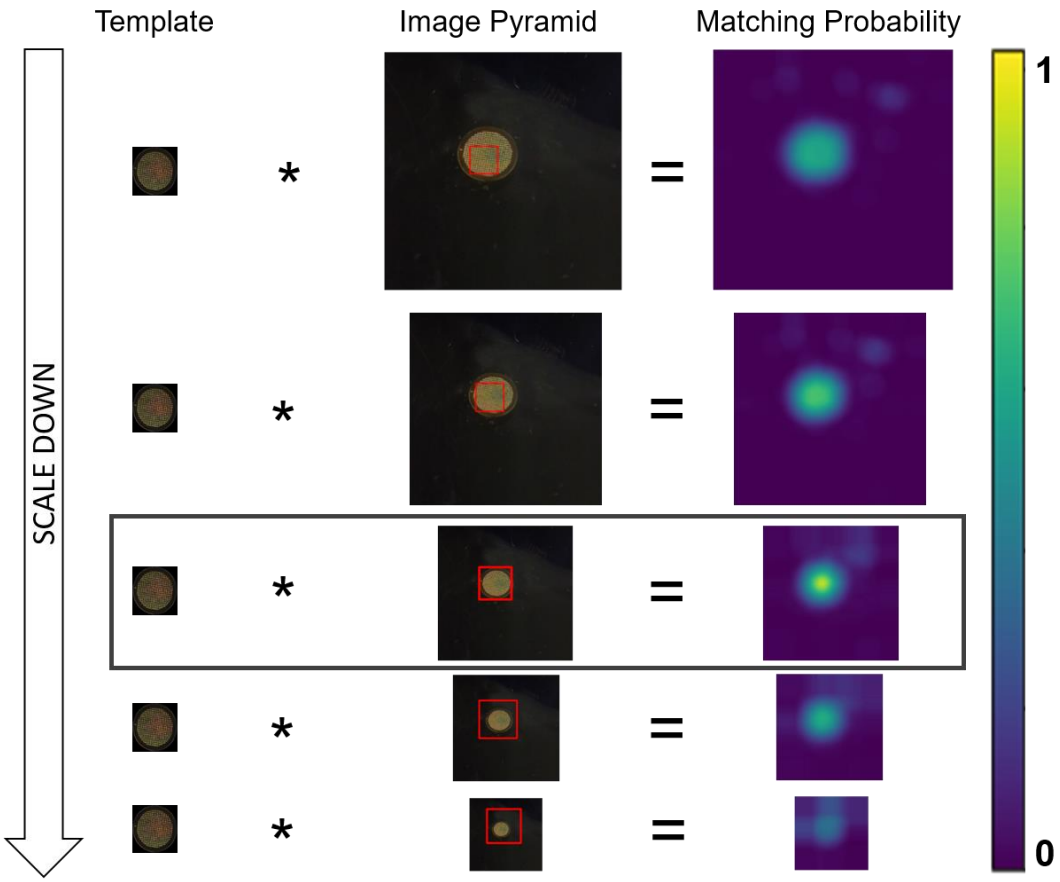

Figure S7. Multi-scale template matching with image pyramid. The size of the template is fixed while resampling input image with different scales. The red boxes mark the best solution determined by the probability value across the scale space. The color bar represents the matching probability.

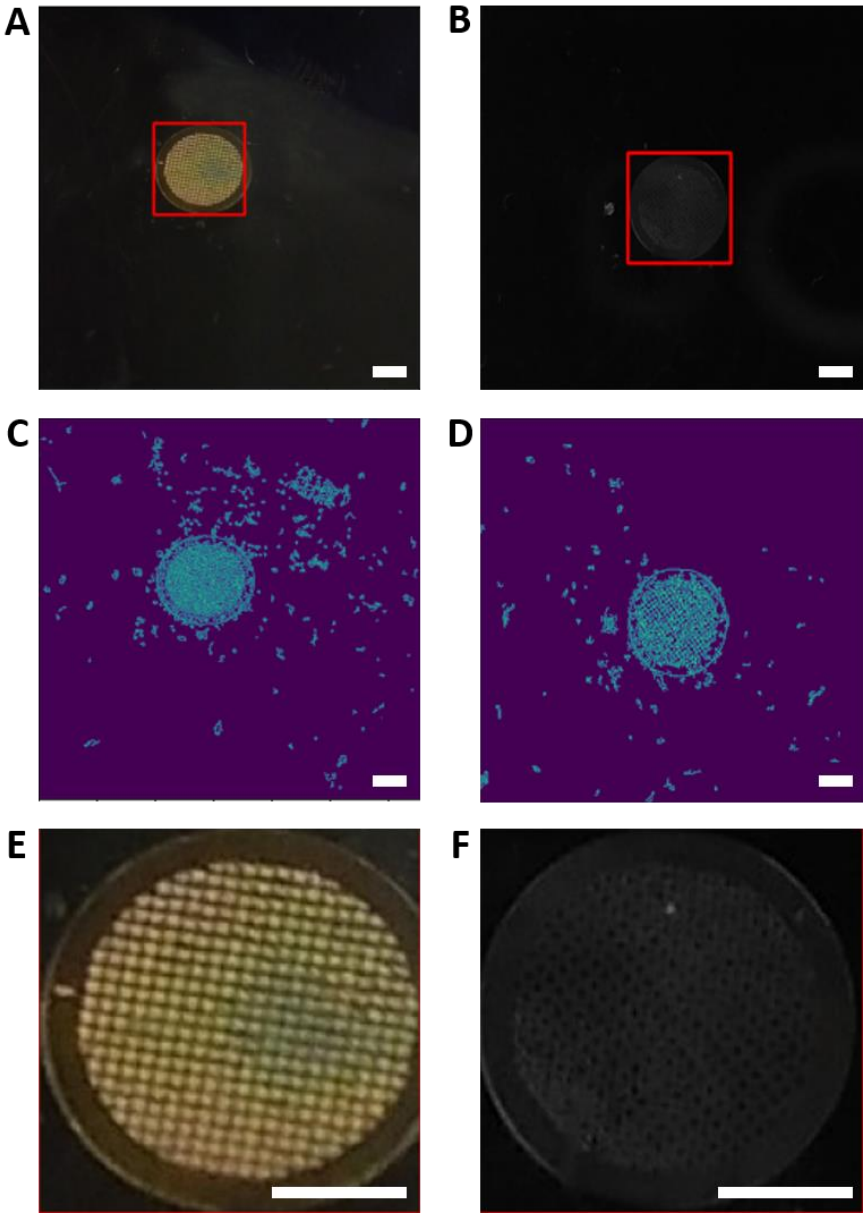

Figure S8. Brightness invariant transformation. (A-B) The image of the LC-infused grid with (A) high and (B) low brightness. Red boxes indicate the location of the LC-infused grid. (C**)** and (D) are the feature map extracted by Canny edge operator from (A) and (B), respectively. (E) and (F) show the corresponding pixel content within the red box of (A) and (B), respectively. Scale bars, 1 mm.

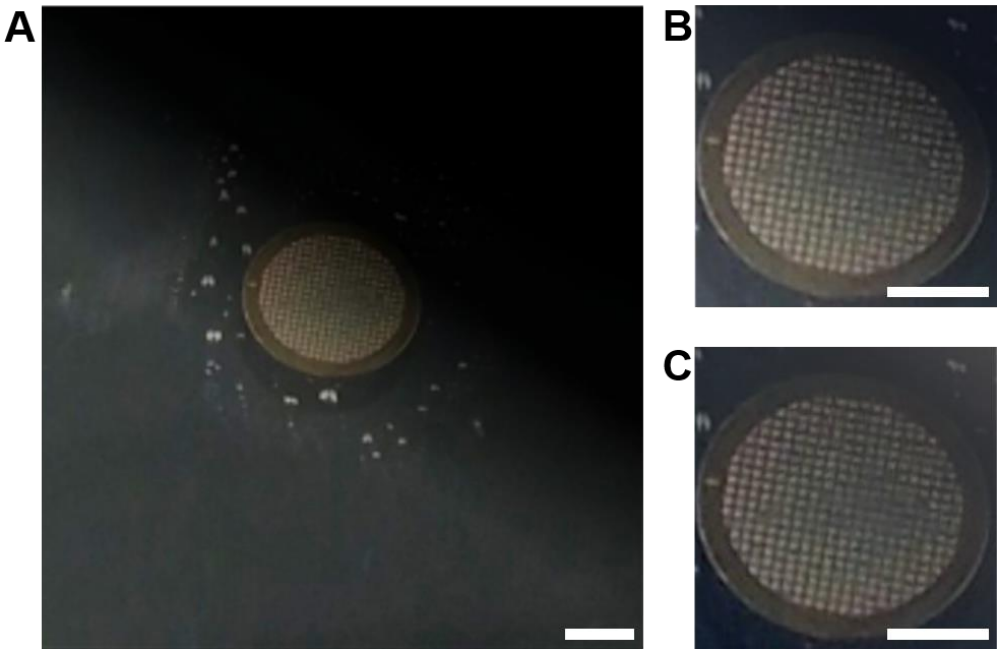

Figure S9. Uneven illumination correction. (A) A representative image of the LC-infused grid under uneven lighting condition. (B) Radiometric correction that subtracts the mean value. (C) Radiometric correction that subtracts the linear model fitted with a least squared estimator. Scale bars, 1 mm.

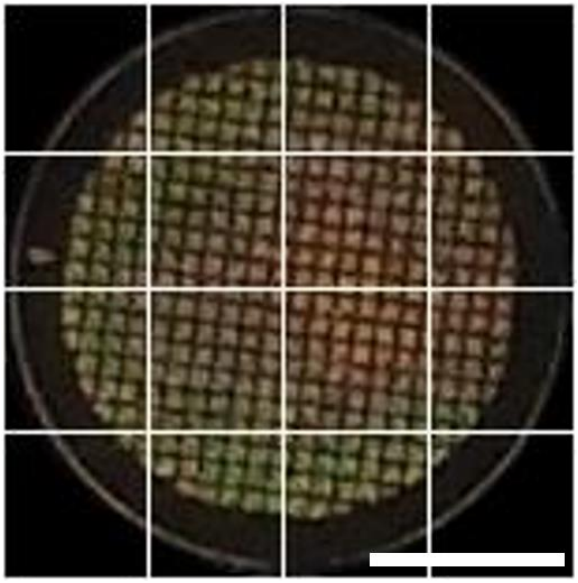

Figure S10. Spatial partition of the Region of Interest (ROI) image in feature transformation. The statistics are computed in each grid and each channel. The grid of values is then transformed to a feature vector by concatenating all values. Scale bar, 1 mm.

Supplemental References

1. Laven, J., and de With, G. (2011). Should the Gibbs analysis be revised? Langmuir *27,* 7958–7962.
2. Menger, F. M., and Rizvi, S. A. (2011). Relationship between surface tension and surface coverage. Langmuir *27,* 13975–13977.
3. Sokołowski, A., Bieniecki, A., Wilk, K. A., and Burczyk, B. (1995). Surface activity and micelle formation of chemodegradable cationic surfactants containing the 1,3-dioxolane moiety. Colloid Surface A *98,* 73–79.
4. Brunelli, R. (2009). Template Matching Techniques in Computer Vision: Theory and Practice (John Wiley & Sons, Hoboken, NJ, USA).
5. Canny, J. (1986). A computational approach to edge detection. IEEE T. Pattern Anal. *6,* 679–698.
6. Bradski, G., and Kaehler, A. (2008). Learning OpenCV: Computer Vision with the OpenCV Library (O'Reilly Media, Inc).
7. Adelson, E. H., Anderson, C. H., Bergen, J. R., Burt, P. J., and Ogden, J. M. (1984). Pyramid methods in image processing. RCA Eng. *29,* 33–41.
8. Joblove, G. H., and Greenberg, D. (1978). Color spaces for computer graphics. SIGGRAPH Computer Graphics *12,* 20–25.
9. Chang, C.-C., and Lin, C.-J. (2011). Libsvm: a library for support vector machines. ACM T. Intell. Syst. Technol. *2,* 1–27.
10. Pedregosa, F., Varoquaux, G., Gramfort, A., Michel, V., Thirion, B., Grisel, O., Blondel, M., Prettenhofer, P., Weiss, R., Dubourg, V., et al. (2011). Scikit-learn: machine learning in Python. J. Mach. Learn. Res. *12,* 2825–2830.
11. Guazzelli, A., Zeller, M., Lin, W. C., and Williams, G. (2009). PMML: an open standard for sharing models. R J. *1,* 60–65.